ABSTRACT

Title of Thesis: EMBEDDED STRAIN SENSOR WITH POWER SCAVENGING FROM BRIDGE VIBRATION

Ming Wang, Master of Science, 2004

Thesis directed by: Professor Peter C. Chang
Department of Civil Engineering

The Objective of this thesis is to investigate an embedded strain sensor system with power scavenged from highway bridge vibration for structure health monitoring. A power scavenging scheme is developed to power the sensor system so as to eliminate the dependence of batteries. Three mechanisms (PZT patch, cantilever beam and PZT stacks/slugs) are described that are suitable for the remote sensor system to scavenge mechanical energy at different locations in a bridge. Calculations and experiments are taken to examine the feasibility of the idea, and predicted power generation is compared to solar/light power. A scheme of an embedded strain sensor using resonant MEMS beam structure is introduced along with the theoretical analysis and simulation. The last consideration is the signal propagation attenuation in concrete. Measurements are taken to

determine the RF signal attenuation at 900 MHz range transmitted through a concrete slab. Theoretical calculations are validated by experimental results.

EMBEDDED STRAIN SENSOR WITH POWER SCAVENGING FROM BRIDGE VIBRATION

by

Ming Wang

Thesis submitted to the Faculty of the Graduate School of the
University of Maryland, College Park in partial fulfillment
of the requirements for the degree of
Master of Science
2004

Advisory Committee:

Professor Peter C. Chang, Chair
Professor Chung C. Fu
Professor Darryll Pines

Table of Contents

List of Figures

List of Tables

Chapter 1

Introduction

The traditional method to ensure the structural safety of civil infrastructure is to do visual inspection regularly. This is a simple but ineffective means since the health of structures can not be diagnosed adequately by its appearance alone. Critical deteriorations or damages often occur inside the structure, for example the corrosion of rebars in concrete. Corrosion initiation and growth are difficult to be perceived and controlled. Research on structural health monitoring for civil infrastructures and space/aircraft transportation system has experienced rapid growth in recent years. For example, accelerometers are placed on a structure, and then the vibration of the structure can be used to determine the condition of the structure. This is a global health monitoring method by observing changes of dynamic properties of the structure. Local monitoring method is to place sensors at some pre-determined hot spots where damage is expected. Both global and local methods need to install sensors in the investigated structure. Useful structural information (e.g.: strain/stress, acceleration, temperature etc.) is then obtained by monitoring those sensors.

The traditional methods of communication between sensors and data collection units rely on wire connections. However not only is the wiring a large number of sensors costly, but also large bundles of wires from different parts of a structure are difficult to manage and they are subjected to environmental deterioration. So, remote wireless technology becomes an attractive means to establish communication between sensors and a central unit.

The concept of wireless monitoring system was introduced in [Straser et al., 1998], and a wireless modular monitoring system (WiMMS) [Lynch et al., 2000] was then developed using economical and commercially available components for implementing the wireless communication of sensor measurements in structures. A WiMMS unit is powered by 3 groups of 6 AA alkaline batteries (18 total), which provides up to 21 days in sleep mode and up to 11 hours for continuous operation [Straser et al., 2000]. SG-Link™ Wireless Strain Gauge System [MicroStrain, Inc.] is a commercially available product which combines full strain gauge conditioning with micro datalogging transceiver system for fulfilling wireless strain monitoring. SG-Link node, as shown in Figure 1.1, is powered by a 3.6 volt lithium ion AA size internal battery which provides up to 230 hours of lifespan.

Figure 1.1 SG-Link node

In this thesis, an embedded sensor system for structural health monitoring of highway bridges is described. This sensor system employs a power scavenging device to harvest energy from the bridge vibration so that the dependence of batteries is eliminated, and the lifespan of the sensor system is then increased. Strain information is obtained by a vibrating beam-type stress sensor and the integrated transmitter sends

those results back to a handheld monitor via radio frequency signals. This realizes the operation of a wireless, self-powered and embedded sensor system for structural health monitoring.

This thesis concentrates on three main aspects: power scavenging from highway bridge vibration, embedded beam-type strain sensor and signal attenuation in concrete.

1.1 Power scavenging from highway bridge vibration

The capability of health monitoring system relies on the performance and reliability of sensors. So sensors should be able to work in a sustained mode and do not need to be replaced or repaired over the life of the structure. Embedded sensors are recently considered as promising means. However, powering these sensor systems is a significant problem since battery power offers only a limited life span, and battery management is inconvenient and impractical. Self-powered sensors are attractive because they allow the sensors to be tetherless. Moreover they make use of the energy from the ambient environment which is usually dissipated as heat and radiation. The harvested energy could be converted into a useful form upon the demand of sensors. The ideal case is that the harvested power is sufficient to provide a constant power supply for the sensor system. This depends on both the amount of power harvested from the environment and the power consumption of the sensors. An alternative way is to store the generated energy and give a power burst to the sensor system when power is needed.

Various approaches have been studied to convert and store energy from ambient energy sources, including solar [Lee et al., 1995], [Warneke et al., 2002], human power [Starner, 1996], radio frequency [Friedman et al., 1997], [Wu et al., 2001], [Jung et al.,

1999], thermal gradients [Glosch et al., 1999] and mechanical vibration [Williams et al., 1997], [Meninger et al., 2001], [Amirtharajah et al., 1998], [Glynne-Jones et al., 2001], [El-hami et al., 2001], [Shearwood et al., 1997].

A successful example of power scavenging is the "parasitic piezoelectric shoe" [Shenck et al., 2001] developed by the MIT Media Laboratory. The "piezoelectric" shoe utilizes PZT uniform and polyvinylidene fluoride (PVDF) stave mounted under an insole as the power generating element; an average of 1.3 to 8mW of power was collected at a 0.9 Hz walking pace. The harvested energy successfully powered an RFID tag system and transmitted an identification signal to local surroundings. Similarly researchers in Sandia National Laboratory have developed piezoelectric-based self-powered sensor tags and proposed the idea to use the sensor tags to monitor the state-of-health of structures [Pfeifer et al., 2001]. The design of a MEMS transducer system that converts ambient mechanical vibration into electrical energy through the use of a variable capacitor was presented in [Meninger et al., 2001]. The feasibility of operating a digital system from power generated through a vibration-based power generator is demonstrated in [Amirtharajah et al., 1998], in which an integrated chip was designed and tested. A thick-film piezoelectric microgenerator and vibration-based electromechamical power generator were introduced and experimental setups described in [Glynne-Jones et al., 2001] and [El-hami et al., 2001], respectively.

With the development of vibration-to-electric energy conversion technology, researchers have begun to think of using energy harvesting means to power the sensors installed in highway bridges, such as accelerometers, strain gages, thermometers, anemometers, and even video monitors. [Williams et al., 1997] presented a feasibility

study of a vibration-to-electric generator designed to generate power from bridge vibration. However it is not clear how much power can be harvested in a highway bridge. This thesis attempts to estimate the power that can be generated quantitatively.

1.2 Embedded beam-type strain sensor

The most common strain sensors are surface mounted resistance strain gauges. Vibrating wire spot-weldable strain gauge [Ace Instrument Co., Ltd.] is designed to be embedded in reinforced concrete to detect strain in concrete or strain in steel rebars. This kind of embedded strain gauge needs shielded cables to transmit the signals out. So the amount of such sensors in a structure has to be restricted in order not to influence the performance of the structure.

In this thesis, a MEMS beam-type strain sensor which can be either mounted on the surface or embedded inside of a structure is investigated. The device is a beam fixed at both ends for which the resonant frequency is determined by its axial strain which is related to its resonant frequency. This kind of strain sensor is more stable than the traditional resistance strain gauges. The linear relationship between strain and frequency is studied by simulating a beam-type device under different axial stresses. The capacitance excitement and detection technologies are also investigated.

1.3 Signal attenuation in concrete

Once an embedded sensor is installed in a bridge, and it is powered by the means of energy scavenging, it is necessary to know if the harvested power is sufficient for the sensor's demand. The attenuation of radio frequency energy is ineluctable when radio

frequency wave transmits through concrete to reach the embedded sensors or when the sensors transmit signals out. For a scheme of power scavenging, the energy harvested by the sensors should be sufficient to complete sensing, data processing and data out-transmitting. If the propagation attenuation is too big, the signal strength sent from transmitter has to be high enough, but sometimes this requirement is infeasible when the power supply is limited. Some empirical and theoretical models have been developed to investigate the influence of construction material such as concrete wall, wood or steel door, windows and so on in modern office building environment [Lafortune et al., 1990], [Honcharenko et al., 1992], [Honcharenko et al., 1993], [Seidelet al., 1994], [Lawton et al., 1994] and [Lawton et al., 1999]. In order to determine the depth at which an embedded sensor can possibly be placed, the attenuation of RF energy through concrete needs to be studied.

In this thesis, chapter 2 introduces the embedded sensor system for structural health monitoring. Chapter 3 describes the simulation of the traffic-induced vibration of a girder bridge model and then investigates three approaches for piezoelectric-based power scavenging based on the simulation results. Power storage considerations and some experimental results are also discussed in this chapter, and the expected power generation is compared to solar power and the power demand estimation of the embedded strains sensor system. In Chapter 4, a resonant MEMS beam strain sensor is studied. The capacitance excitement and detection technologies are also discussed. In chapter 5, the measurement of propagation attenuation through concrete at 900 MHz range was presented. Chapter 6 concluded this thesis with summary of results and insights and indicates areas of future research.

Chapter 2

Embedded Sensor System for Structural Health Monitoring

Strain sensors often need to be embedded inside the structure to measure local strain of the structural components such as reinforcement steel. The goal of this research is to investigate the possibility of using an embedded sensor system for health monitoring of highway bridges. The sensor system consists of a sensor module, a power scavenging module, a system controller module and a transceiver module. The sensor module takes measurements of structural information such as strain. The power scavenging module is to harvest energy from ambient sources such as highway bridge vibration, and the harvested energy is stored in a power storage device. This module provides the power demand for the sensor system. The system controller module controls the operation modes of the system including sleeping mode and working mode. The transceiver module has two functions: receiving command signals from a handheld monitor and transmitting information of structures back to the handheld monitor. The system block diagram is shown in Figure 2.1.

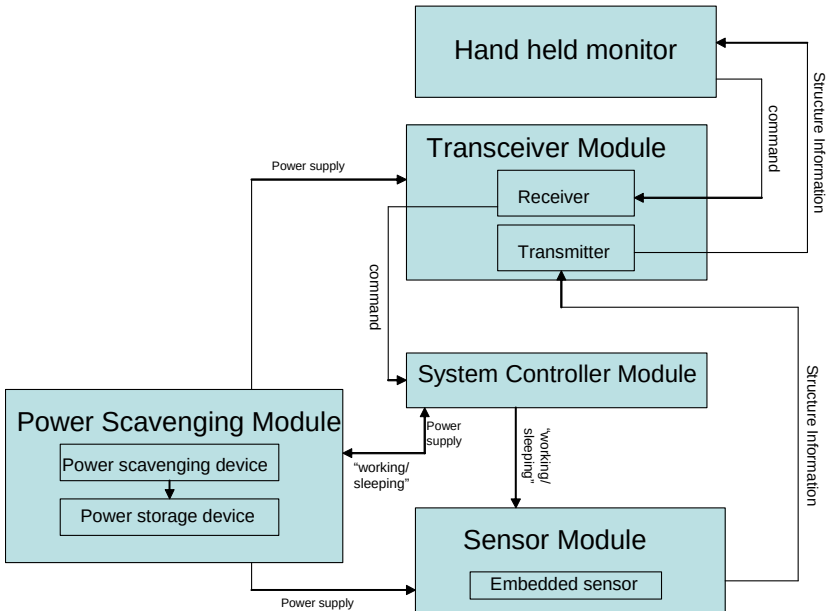

Figure 2.1 Block diagram of embedded sensor system

Without commands from handheld monitor, the sensor system is in “sleeping” status. The power scavenging module provides a constant power for receiver and system controller module to be sustained in a “waiting” status. When the receiver gets a “wake up” command signal from the handheld monitor, the system controller module gives “working” commands to the sensor and power scavenging modules. The power scavenging module provides sufficient power for the demand of the sensor module and the transceiver module by discharging the power storage device. The embedded sensor starts to collect structure information and the transmitter sends those results back to the handheld monitor. When the handheld monitor obtains the expected information, it sends a “sleeping” command out, and the sensor system goes to “sleeping” mode. The collected information is either stored in the handheld device or sent to a central unit for advanced analysis.

The sensor system has three main advantages:

- Wireless
- Embedded in structures
- Self-powered

Since the operation of the embedded sensor system relies on the power supplied by the power scavenging module, Chapter 3 gives the estimation of expected power generation from bridge vibration, and compares it to solar power. Finally, the power demand estimation of the sensor system is also given for comparison.

Traditional resistance strain gauges drift significantly in even short periods of time, so they are not suitable for the purpose of long-term monitoring. Chapter 4 introduces a MEMS resonant beam-type strain sensor which is more stable, and it can be embedded and it is wireless. Excitation and detection methods are also investigated.

Since the embedded sensor system is designed to be placed inside of a structure, the signal attenuation has to be considered when the transceiver module sends a signal out or receives a signal from handheld monitor. Chapter 5 investigates the signal attenuation problem by doing measurement.

Chapter 3

Power Scavenging from Highway Bridge Vibration

3.1 Bridge Vibration

Highway bridges vibrate considerably because of vehicle loading and wind. This mechanical energy is dissipated to the environment as heat. In order to determine the amount of mechanical energy that can be harvested, a typical T-shape girder bridge model was developed using ANSYS [ANSYS, Inc., 1998] and the dynamic characteristics of the bridge were obtained by modeling the passage of trucks.

A typical single span bridge is assumed. It is supported by three T-shape girders, and it is assumed to be simply supported at both ends. The traffic on the bridge consists of two lanes with a single lane in each direction as shown in Figure 1. The span length, L, is 88 feet and the deck thickness is 7 inches, which represents a typical highway overpass bridge. The height of the T-shape girder is 65 inches and the thickness is 8 inches. The span space, S, is 10 feet.

The truck wheel load is considered as a three-axle truck (36KN-142KN-142KN) as described in AASHTO Standard (HS20-44 Loading). Figure 3.2 shows the truck loading model. Assume the trucks speed to be 96 km/hour (60 mph). At this speed a wheel takes approximately 1 second to cross this single span.

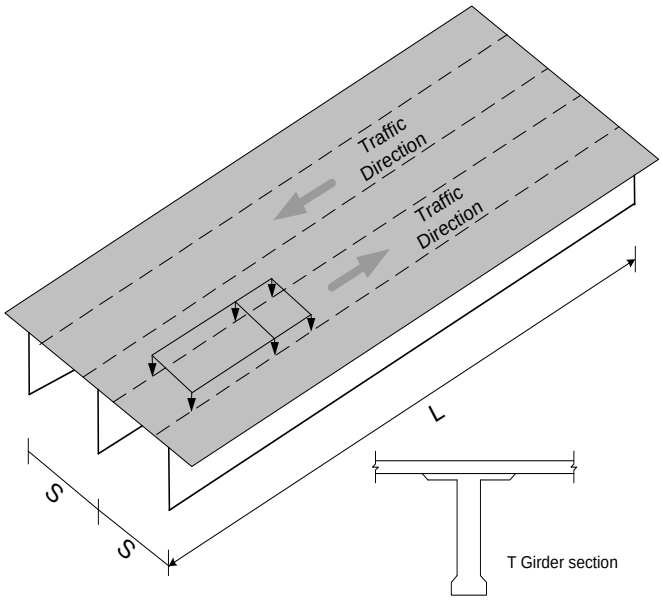

Figure 3.1 Schematic drawing of girder bridge and truckload model

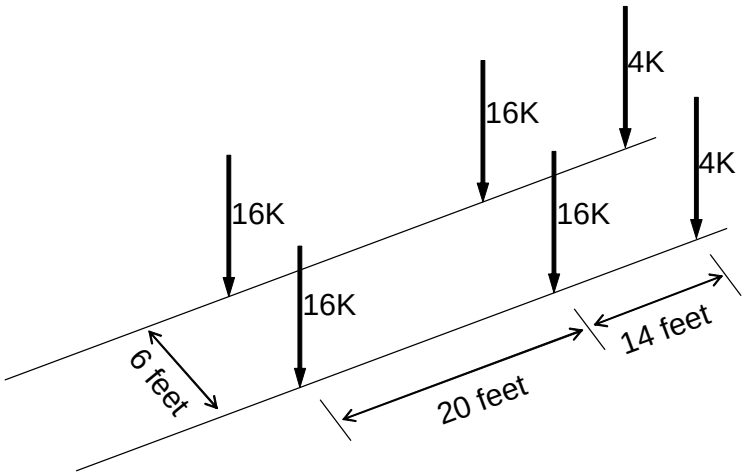

Figure 3.2 Truckload model used in ANSYS

A four-node isoparametric shell (Shell 63) [ANSYS, Inc., 1998] is chosen as the structure element in ANSYS. Both modal and transient dynamic analyses were performed. Figure 3.3 shows the finite element mesh used.

The modal analysis shows that the natural frequency of the first mode is 8.51 Hz. Table 3.1 shows the first five modes of vibration. Figure 3.4 gives the first four vibration mode shapes.

Transient dynamic analysis is performed to determine the dynamic response of the structure under the action of the moving truck. The dynamic displacement of an interior girder was obtained from the transient dynamic analysis. Figure 3.5 (a) and (b) shows the time-history displacement at the mid-span point and a point 2 feet from the left support, respectively. Figure 3.6 (a) and (b) show their dynamic strains.

Table 3.1 Modal analysis results

1st mode	2nd mode	3rd mode	4th mode	5th mode
8.51Hz	8.56Hz	12.14Hz	17.71Hz	19.35Hz

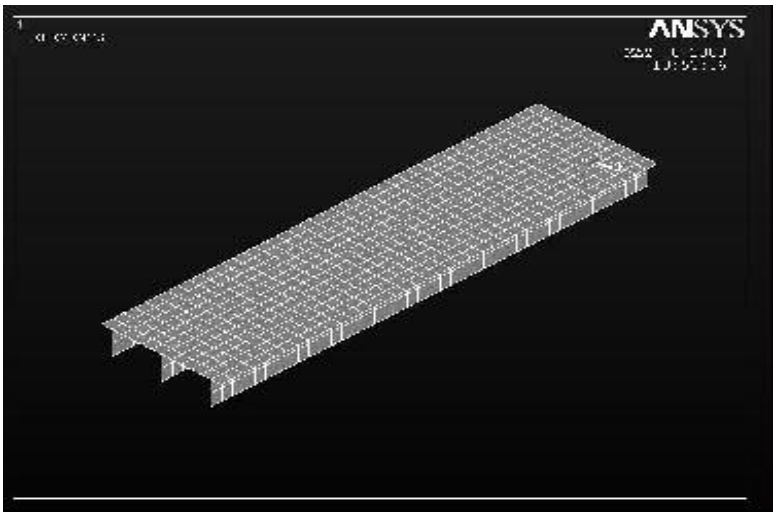

Figure 3.3 Finite element mesh plot

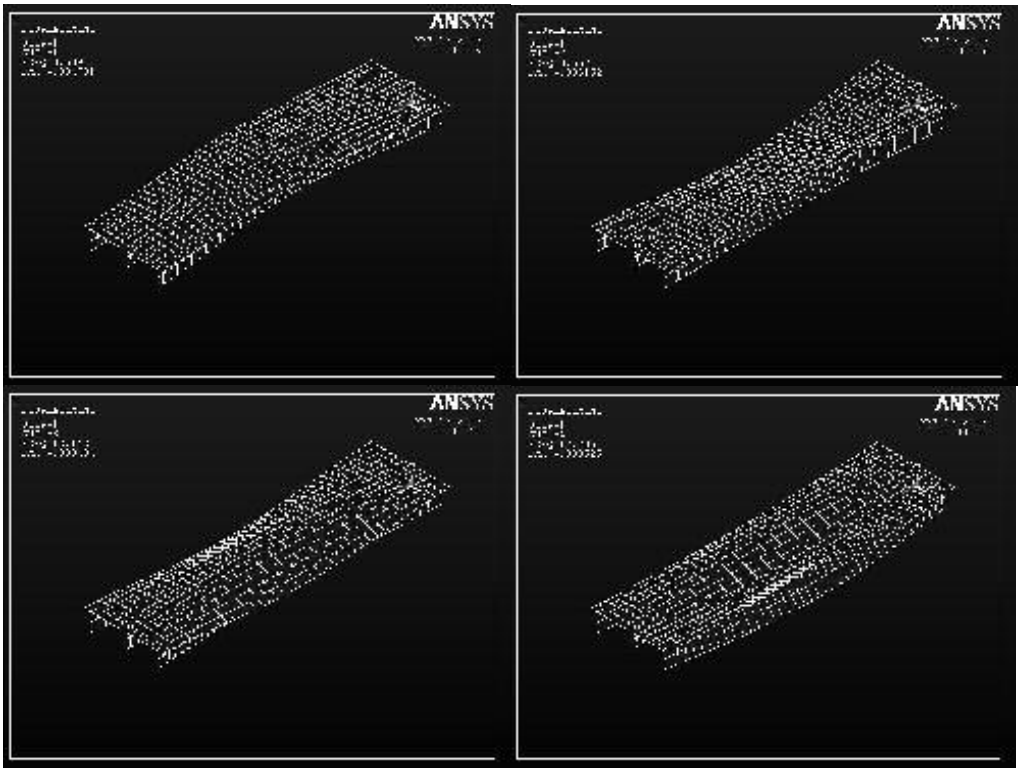

Figure 3.4 First four vibration mode shapes

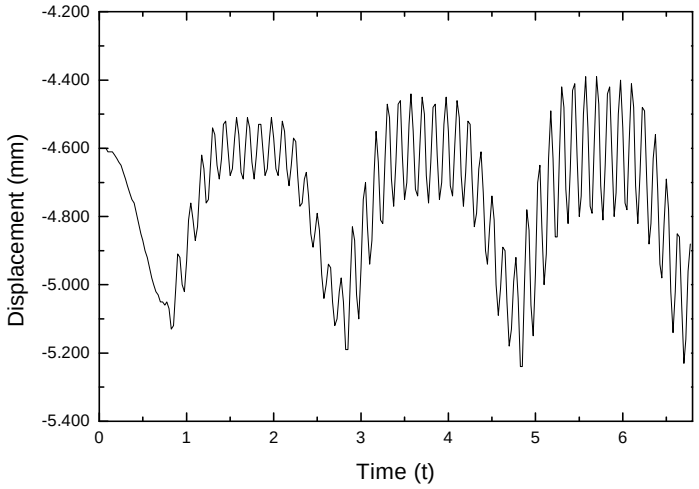

(a)

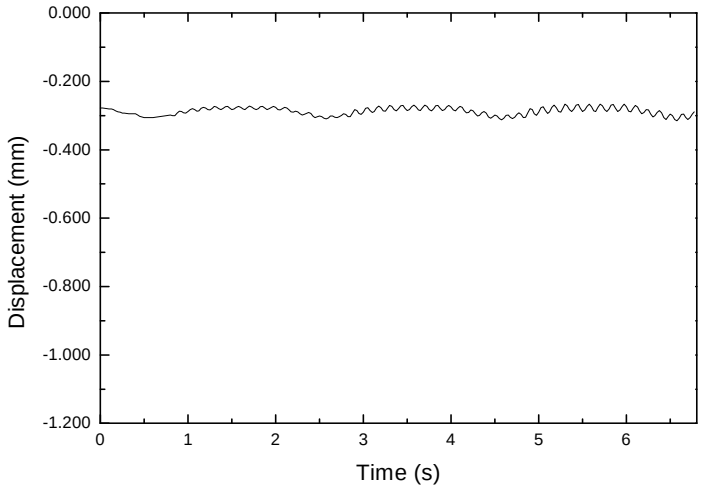

(b)

Figure 3.5 Dynamic displacement of girder, (a) vertical displacement at mid-span and (b) vertical displacement at a point 2 feet from support

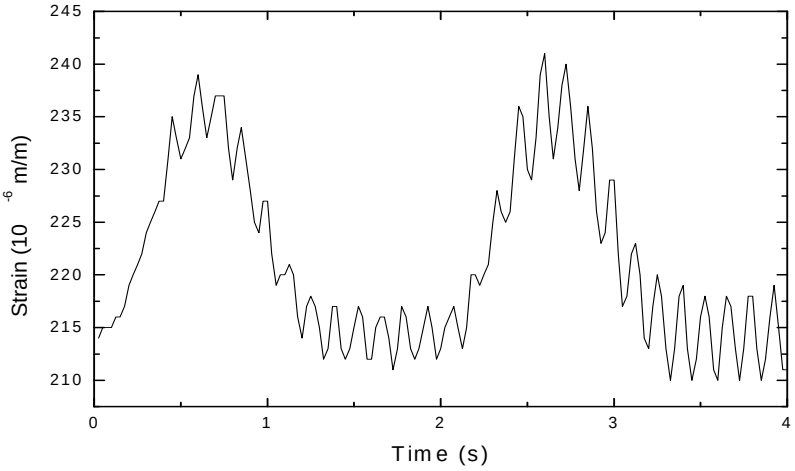

(a)

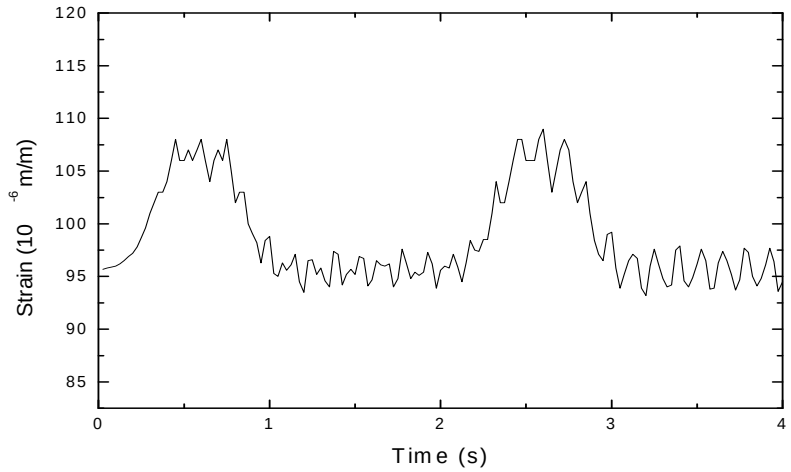

(b)

Figure 3.6 Dynamic strains at (a) mid-span and
(b) a point 2 feet from support

These results show that the dynamic responses consist of two parts. One part corresponds to the bridge's free vibration which corresponds to the higher frequency

signals (around 8 Hz), and the other part corresponds to the truckload-induced vibration which appears as the higher amplitude signal with lower frequency (around 0.8 Hz).

3.2 Approaches for Power Scavenging

The idea of energy scavenging here is to employ a piezoelectric structure as the power generation element. Piezoelectric materials generate an electricity when subjected to a mechanical deformation; and vice versa. The piezoelectric materials such as PZT (lead zirconate titanate), ZnO, Quartz, PVDF (polyvinylidene fluoride) etc. have been widely used as sensors and actuators. In [Weinberg, 1999] the solutions of working equations for a piezoelectric beam are derived.

In this thesis, three types of approaches are studied: patch, cantilevered beam, and stacks/slugs. They are suitable for harvesting different kinds of mechanical energy in a bridge: structural strain, vibration, and impact compression.

3.2.1 Piezoelectric Phenomenon

Piezoelectric phenomenon was first discovered in 1880s by Pierre and Jacque Curie. They found that some crystalline materials generate a voltage when compressed (generator effect) and change shape when an electric field is applied (motor effect). Although some natural materials (eg: quatz) are found to show piezoelectric effects, most modern piezoelectric devices are made with artificial polycrystalline ceramics such as PZT (lead zirconate titanate), which is considered in this thesis. Piezoelectric properties are directionally dependent. Figure 3.7 shows the 33 and 31 operation modes under generator effect. P denotes the polarization direction of the PZT material.

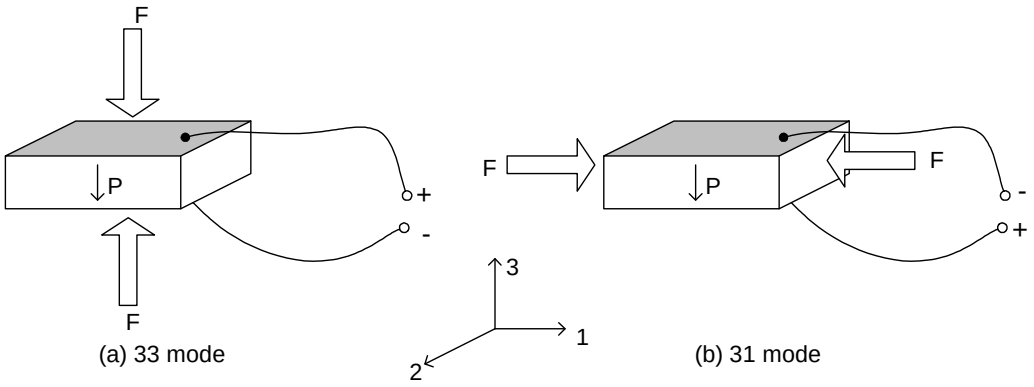

Figure 3.7 Piezoelectric sensor operation modes

The piezoelectric behavior can be described by the following equations:

$$D_{ij} = d_{ij} X + \varepsilon E \tag{3.1a}$$

$$S_i = sX + d_{ij} E_i \tag{3.1b}$$

The index i indicates that the electrodes are perpendicular to axis i, and index j indicates that the piezoelectric induced strain or the applied stress is in the direction j. D is electrical displacement along polarization axis, and S is strain. d_{ij} is defined as piezoelectric strain coefficient. ε is the dielectric constant of the material. E is the electric field generated between electrodes. X is mechanical stress developed in piezoelectric material. s is mechanical compliance in a constant electrical field. Equation 3.1a reflects the generator effect and equation 3.1b reflects the motor effect.

3.2.2 PZT Patch

The patch configuration is the most direct and simple means to convert bridge vibration into power. PZT patches can be placed on the surface of girders, usually on top

of a flange or on the bottom of a slab, where the strain change is high relative to other locations. At these locations, the PZT patches are subjected to stress changes due to traffic loads. If the bond between the PZT patch and concrete transfers the deflection perfectly, the attached PZT patch has the same strain as the girder. Figure 3.8 (a) and (b) show the strain change at the mid-span point on the bottom of girder and at the point close to the support, respectively. The strain change in the PZT patch can be divided into two parts: (1) traffic-induced strain and (2) free vibration strain. The traffic-induced output has the properties of high amplitude but low frequency (26 micro strain and 0.77 Hz). The free vibration output has the properties of low amplitude but relatively high frequency (4 micro strain and 8 Hz). The total power harvested by the PZT patches is from the combination of these two vibration sources. Here a low-pass filter is used to obtain the truck-induced vibration and a high-pass filter used to obtain the free vibration. Then the power generation from these two vibration sources is calculated. Figure 3.9 shows the vibration signals after the filters.

If a 10cm×10cm×0.2cm PZT patch with mechanical and piezoelectric properties shown in Table 3.2 is used, the harvested power can be estimated.

Table 3.2 PZT (PSI-5A-S4-ENH [Piezo Systems, Inc.]) material properties

$\mathbf{d_{31}}$ (m/volts)	$\mathbf{g_{31}}$ (volt·m/N)	$\boldsymbol{\varepsilon_3}$	$\mathbf{k_{31}}$	$\boldsymbol{\rho}$ (Kg/m)	$\mathbf{E_{11}}$ (N/m^2)	$\boldsymbol{\nu}$
-190E-12	-11.6E-3	1800	0.32	7800	6.6E10	0.31

d_{31}: piezoelectric strain coefficient
g_{31}: piezoelectric voltage coefficient
ε_3: relative dielectric constant between poling electrodes
k_{31}: coupling coefficient
ρ: density
E_{11}: elastic modulus in longitude
ν: Poisson's ratio

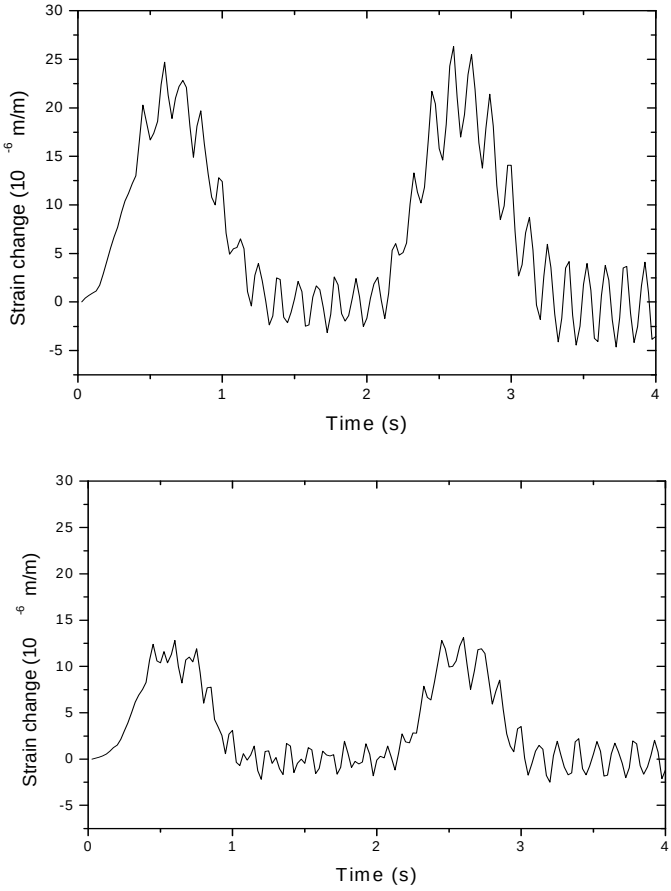

(b)

Figure 3.8 Strain changes of girder bottom at (a) mid-span and (b) the point which is 2 feet to the left support

3.2.2.1 Power generation from truckload-induced strain

This part of the time-history of strain change can be considered as a periodic signal with frequencies around 0.5 Hz which is shown in Figure 3.9. The generated open circuit voltage from the PZT patch can be written in terms of strain:

$$V_{open} = \varepsilon_s E_{11} g_{31} T \tag{3.2}$$

where ε_S is the longitudinal strain of the patch. T is the thickness of the PZT ceramic layer.

From Figure 3.9, the maximum strain of the truck-induced vibration ε_s=21 micro strain. Substituting it into (3.2), the maximum open circuit voltage is approximately 31.5 volts. Then the average energy generated in the PZT patch can be calculated based on the peak voltage output:

$$E_e = \frac{1}{2} C V^2 \tag{3.3}$$

C is the capacitance of the PZT patch which is determined by

$$C = \frac{\varepsilon_0 \varepsilon_3 A}{T} \tag{3.4}$$

A is the surface area of the electrode. In this case, A is equal to 100 cm^2. ε_3 is the relative dielectric constant between poling electrodes and ε_0 is the permittivity of vacuum. (ε_0=8.85×10^{-12} farads/m)

From (3.4) the capacitance of the single PZT patch is about 80 nF. The available energy then is calculated from (3.3):

$$E_e = \frac{1}{2} \cdot 8.0 \times 10^{-8} \, Farad \cdot (31.5 volts)^2 = 4.0 \times 10^{-5} \, J = 40 \, \mu J$$

The average available power in the 0.5Hz vibration is then:

$$P_e = 2 \times f \times E_e = 2 \times 0.5Hz \times 4.0 \times 10^{-5} J = 40 \mu W$$

f is frequency in Hz, and f is equal to 0.5Hz in this case. The area of the PZT patch is 100cm^2. So the power density is about 0.4μW/cm^2.

The output power can also be determined by connecting a test resistance to the patch device. The output power can be written: [Kendall, 1998]

$$P_o = \frac{(\varepsilon_S A \omega E_{11} d_{31})^2 R}{(1 + (\omega C R)^2)} \tag{3.5}$$

where ω=2πf, and R is the test resistance.

If the maximum strain from Figure 3.9 (ε_s=21 micro strain) is substituted into to (3.5), the peak power output can be obtained at an optimized test resistance. Figure 3.10 illustrates the peak power output versus test resistance, and it shows that the peak power is around 124 μW at 3850 K Ohms.

If the optimized test resistance (R=3850 K Ohms) is substituted into (3.5), and use the time-history strain change to replace ε_s, the instantaneous power can be obtained, and is shown in Figure 3.11. The average power output is about 33 μW, which is close to 40 μW estimated by equations 3.3 and 3.4.

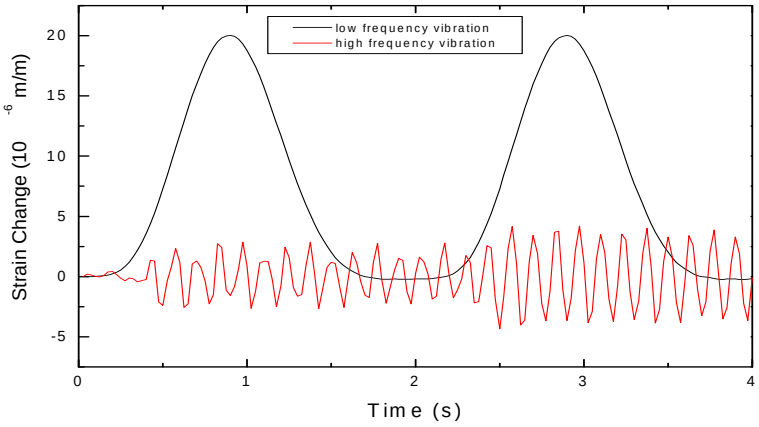

Figure 3.9 Vibration signals after filters (mid-span location)

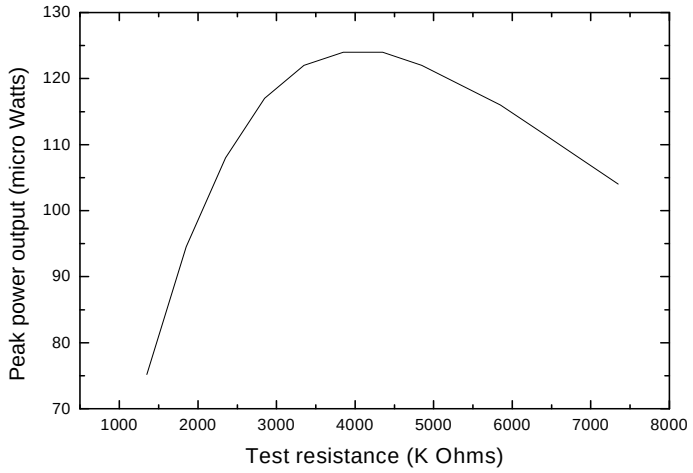

Figure 3.10 Peak power output under different test resistance load (for low frequency vibtation)

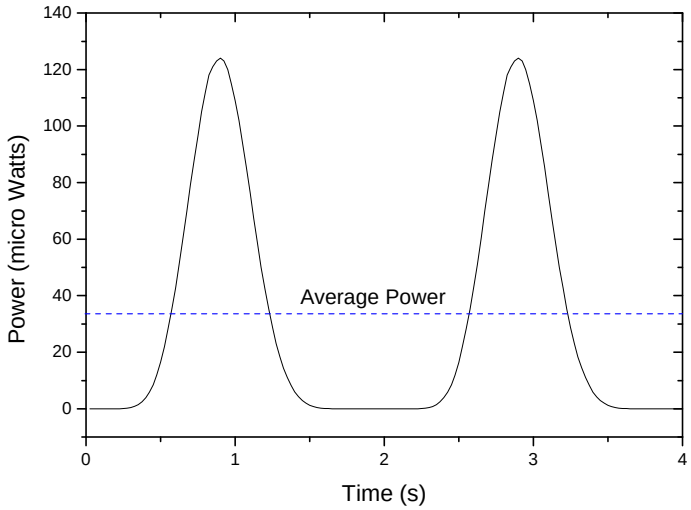

Figure 3.11 Instantaneous power under 3.85M Ohms load
(for low frequency vibration)

3.2.2.2 Power generation from strain induced by free vibration

The part of free vibration can be considered as a periodic signal with frequency 8.51 Hz shown in Figure 3.9. Following the same procedure as described in section 3.2.2.1, the PZT single patch generates a peak power of about 100 μW at 281 K ohms as shown in Figure 3.12, and an average power of 22 μW as shown in Figure 3.13.

The results show that both low frequency and high frequency vibrations have contributions to the power generation. Under optimized resistive loads, the total available power from the PZT device is around 55 μW. If the PZT patch is placed on the bottom of the interior girder at 1/4 span, the total available power output is around 25 μW.

The harvested power is related to the size of the PZT patch. Making the single patch thicker will increase the power output. A thick PZT patch is commercially

available. For example, Morgan Electro Ceramics Ltd. supplies PZT sheets with thickness ranging from 0.2mm to 15mm [Morgan Electro Ceramics].

Although the strain in the girder is relatively high (up to 300 micro strain), the strain change due to traffic is relatively low (<30 micro strain). That is why the PZT patch seems not to be an effective way to scavenge power according to the above results. However the patches have their own advantages in that the electrical output from them is proportional to the strain on the girders. This is like the function of strain gauges. The maximum voltage or power output is connected to the maximum strain which is important for health monitoring purposes. For example, once the output voltage jumps over a pre-determined value, it can be recorded or transmitted out to a central unit by discharging the stored power in the capacitor.

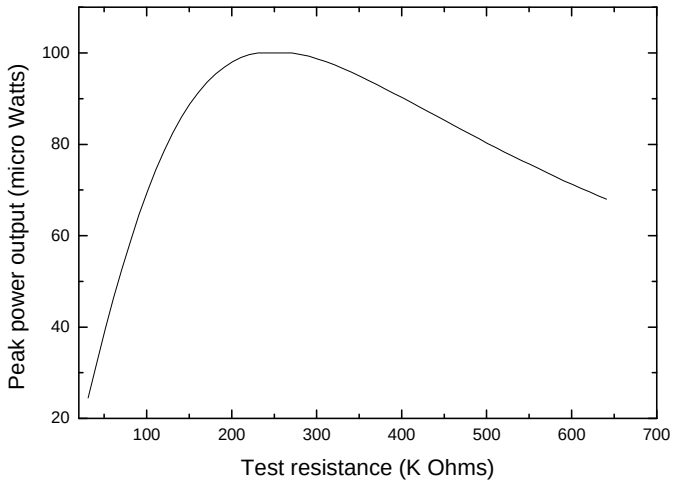

Figure 3.12 Peak power output under different test resistance load (for high frequency vibration)

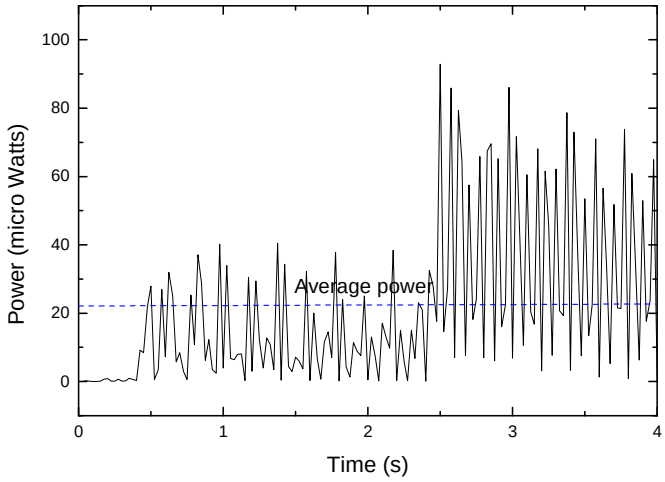

Figure 3.13 Instantaneous power under 281 K Ohms load
(for high frequency vibration)

3.2.3 Cantilever Beam with Tip Mass

Figure 3.14 (a) is the schematic drawing of a cantilever beam structure with a tip mass. The tip mass changes the natural frequency of the beam structure.

The model of the beam structure can be simplified since the weight of the beam is small enough to be neglected compared to the tip mass. Figure 3.14 (b) and (c) show that the clamped end is subject to a motion u(t), and y(t) is the displacement of the free end. The equilibrium equation of the beam system is:

$$m\ddot{y} + c\dot{y} + ky = -m\ddot{u} = P(t) \tag{3.6}$$

m is the mass at the free end; c is the mechanical damping coefficient and k is the stiffness coefficient.

Equation 3.6 shows that the problem of the cantilever beam structure vibration due to the excitation of the fixed end can be considered as the cantilever beam excited by a external force $P(t) = -m\ddot{u}(t)$ applied at the free end, see Figure 3.14 (c).

The excitation force can be obtained from the data of structural dynamic response. This is a second-order continuous-time system and it can be described in the canonical differential equation form:

$$\ddot{y} + 2\zeta\omega_n\dot{y} + \omega_n^2 y = -\ddot{u} \tag{3.7}$$

where $\omega_n = \sqrt{k/m}$ and $\zeta = c/2m\omega_n$. u(t) can be obtained from a finite element simulation described previously and Figure 4 shows u(t) at the mid-span point and the point near the support. All the data are the nodal displacement in the vertical direction.

One example implementation of the cantilever-type generator is shown in Figure 3.15. The substrate (including the tip mass) is made of steel and a PZT layer is deposited on it. The fixed end is attached to a bridge girder and the dynamic displacement of the bridge makes it vibrate. So the PZT ceramic layer on the beam is subjected to dynamic strains. The strain in the PZT layer can be higher than directly mounting the PZT patch onto the girder as the tip mass may amplify the strain caused by the girder vibration. This kind of cantilever beam structure has been studied in [Kovács et al., 2001] as the prototype for an accelerometer.

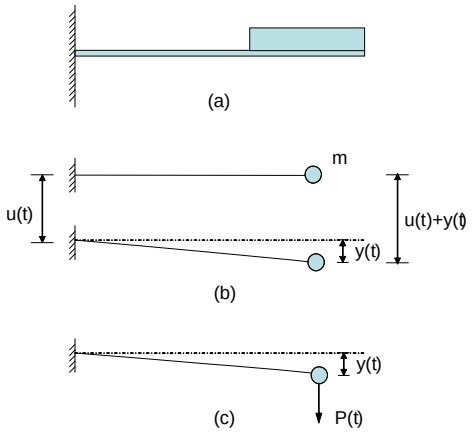

Figure 3.14 Schematic drawing of cantilever beam with tip mass

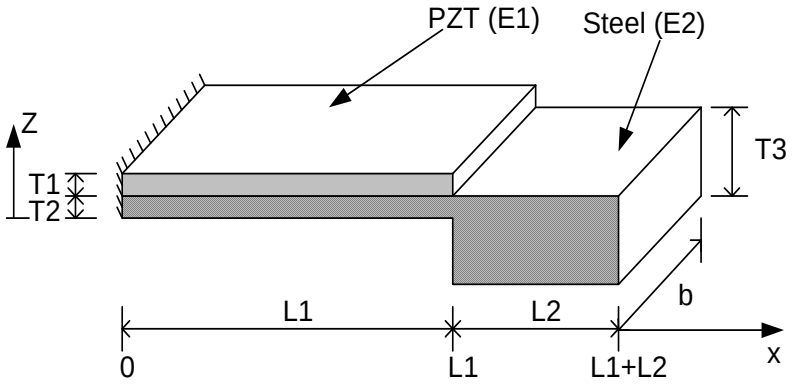

Figure 3.15 Schematic drawing of cantilever-type generator

As an example, a cantilever beam device with L_1=50mm, L_2=30mm, T_1=0.2mm, T_2=0.3mm, T_3=23mm and b=30mm is considered. Its stiffness coefficient is:

$$k = \frac{3EI}{(L_1 + \frac{L_2}{2})^3} \tag{3.8}$$

where E and I are the Young's modulus and the moment of inertia of the two-layer cantilever beam.

$$E = \frac{E_1 T_1 + E_2 T_2}{T_1 + T_2} \tag{3.9}$$

$$I == \frac{b}{12}(T_1^3 + T_2^3) + bT_1(T_2 + T_1/2 - z)^2 + bT_2(z - T_2/2)^2 \tag{3.10}$$

z denotes the distance from the bottom of the beam to its neutral axis. In order to determine E and I, the position of the neutral axis of the two-layer beam needs to be determined. z can be written as [Weinberg, 1999]:

$$z = \frac{E_1 T_1 (T_2 + T_1/2) + E_2 T_2 (T_2/2)}{E_1 T_1 + E_2 T_2} \tag{3.11}$$

The natural frequency of the cantilever beam is given by [Kovács et al., 2001]:

$$f_n = \frac{\omega_n}{2\pi} = \frac{1}{2\pi}\sqrt{\frac{3EI}{\rho_s L_2 b T_3 (L_1 + L_2/2)^3}} \tag{3.12}$$

where ρ_s is the density of the substrate layer. For the dimension chosen for the example cantilever, the stiffness coefficient is found to be 572 N/m, and its natural frequency is about 11Hz.

In [Williams et al., 1997], it is mentioned that u(t) can be transformed into a sum of sinusoids by using a Discrete Fourier Transform algorithm, then average power is derived by solving the differential equation 3.7. Here the differential equation 3.7 is solved with the help of MATLAB [MathWorks, Inc.]. u(t) is the displacement of the mid-span point from 0 to 1.5 second shown in Figure 3.5(a). The tip mass displacement y(t) due to beam distortion was calculated and the result is shown in Figure 3.16.

The strain in the PZT layer is given by:

$$\varepsilon_s(x) = \frac{k(L_1 - x + L_2)(T_1 + T_2)}{2EI} y(t) \tag{3.13}$$

where x is the distance from the fixed end. The average strain is taken as the strain at $x=L_1/2$ in the PZT layer as shown in Figure 3.15. The average energy generation can be written in terms of average strain ε_s:

$$P_e = f_n g_{31} d_{31} L_1 b T_2 E_1^{\ 2} \varepsilon_s^{\ 2} \tag{3.14}$$

For a 5cm×3cm×0.02cm PZT ceramic layer deposited on the steel cantilever beam, the average generated power is:

$$P_e = 11.5 \times 11.6 \times 10^{-3} \times 190 \times 10^{-12} \times 5 \times 10^{-2} \times 3 \times 10^{-2} \times 0.02 \times 10^{-2} \times (6.6 \times 10^{10})^2 \times (100 \times 10^{-4})^2 = 330 \mu W$$

The size of the cantilever beam is about 8cm by 3cm. So the power density is around 14 $\mu W/cm^2$. Figure 3.17 illustrates that the peak power is 1.1 mW at 120 KOhms.

Thicker PZT ceramic layer generates more power. But if the deposited PZT layer is too thick, the stiffness of the cantilever beam becomes high so that it will not develop much strain under excited vibration. To obtain the optimal thickness of PZT ceramic layer T_3 for energy harvesting, the power obtained through the cantilever vibration is expressed in T_3. Figure 3.18 shows the power scavenged as a function of the thickness of PZT layer. The maximum power is about 330 μW, and the optimal thickness is 0.2mm.

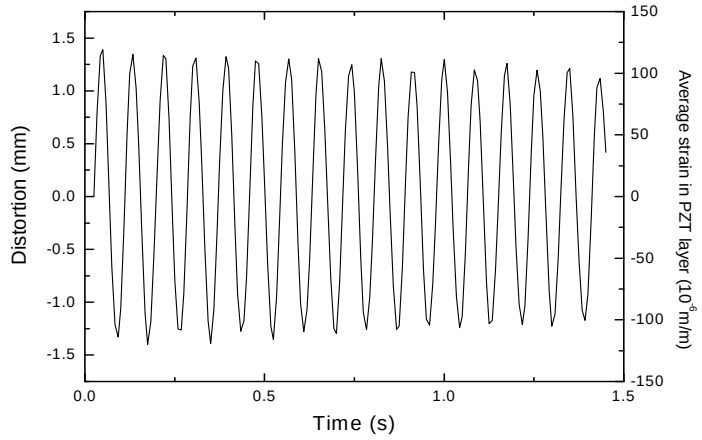

Figure 3.16 Beam distortion y(t) at tip and strain in PZT layer

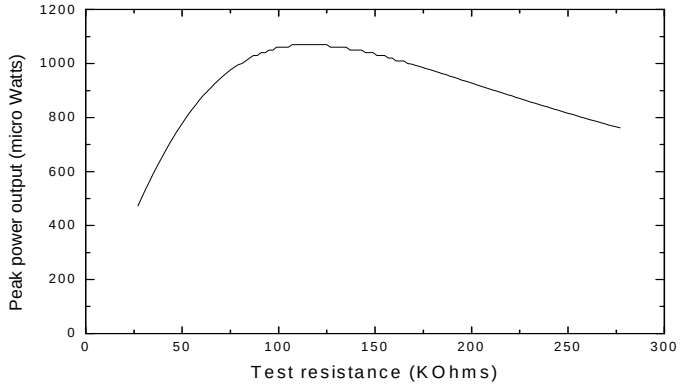

Figure 3.17 Peak power output under different test resistance load

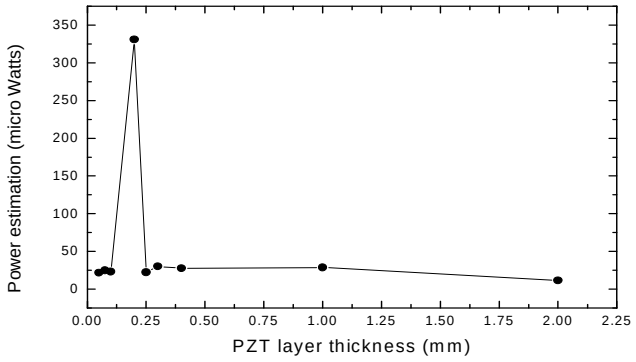

Figure 3.18 Power estimation with different PZT layer thickness

3.2.4 PZT Stacks/Slugs

Vehicle wheels give high impact forces on the bridge deck when they move on a bridge. This results in a compressive stress change between the decking and the girders. PZT stacks or slugs can be placed on the top of girders to sense this vehicle-induced compressive stress. Every time a vehicle moves over the point where a stack/slug of piezoelectric material is embedded, the stack/slug is subjected to an impact compressive force and generates a power impulse. Figure 3.19 shows the compressive stress change at the mid-span point when a 4.8-ton two-axle truck moves over the girder bridge.

Single-layer piezoelectric stacks/slugs are usually used as elements for generating high voltage [Morgan Electro Ceramics, 2000]. One application is the “Igniter” [Sensor Technology Ltd.] which generates a high voltage due to an impact, and this high voltage is applied to an air gap to generate an arc. The operation of the stack/slug generator considered here is similar to the “Igniter.” Vehicle wheels push PZT stack/slugs to generate electric power. However high charge, not high voltage, is more desirable in generators. Multilayer PZT stacks are suitable for high stress environments and for

harvesting large volumes of charge. Figure 3.20 shows a multilayer stack. The open voltage and capacitance are [Piezo Systems, Inc.]:

$$V_{s\_open} = \frac{T_s g_{33} \sigma_s}{N} \tag{3.15}$$

$$C_s = N \frac{\varepsilon_0 \varepsilon_3 A_s}{t_s} \tag{3.16}$$

T_s is the total thickness of the stack. N is the number of layers. g_{33} is the piezoelectric voltage coefficient in the thickness direction. σ_s is the stress in the thickness direction, and $\sigma_s=F/A_s$. A_s is the cross section area of the stack. t_s is the thickness of a single layer.

The values in Figure 3.19 show that the compressive stresses on the top of the girder are not high. Higher impact force on a PZT stack/slug generates more electric energy. So a high stress on the PZT stack/slug generator is expected. A way to amplify the stress is to increase the vertical stress by using a piston type stress concentrator as shown in Figure 3.21. The stress on the stack/slug can be calculated by:

$$\sigma_s = \frac{A_{amp}}{A_s} \sigma_c \tag{3.17}$$

A_{amp} is the top area of stress amplification piston. σ_c is the traffic-induced vertical stress on the piston.

A 1cm diameter×2cm long 10-layerPZT stack with $g_{33}=24\times10^{-3}$m/Volt (PSI-5A-S4-ENH [Piezo Systems, Inc.]) is considered. Assume $A_{amp}=100cm^2$ (10cm×10cm), $\sigma_c=92$KPa from simulated results. The open voltage and stack capacitance can be calculated from equation 3.15 and 3.16: $V_{s_open}=563$Volts and $C_s=6.25$pF. So the available energy is obtained from equation 3.3: $E_s=1$mJ. Assuming the vertical

compressive stress on the stack reaches its peak value every 2 seconds, the available power generated from the PZT stack is 1 mW.

The results show that the power generated in the PZT stack is relatively high when a stress amplification scheme is used, because when cars or trucks move across a bridge, the impact force between wheels and pavement is high. The high impact force on the PZT stacks placed in pavement can generate a relatively high power for a short duration. However, the high impact force may break the PZT stacks (compressive strength=0.5GPa for PSI-5A-S4-ENH [Piezo Systems, Inc.]). Figure 3.22 shows a scheme of stack array. This PZT stack array maybe also be used to sense the wheel impact force and the displacement of the stacks can be controlled by restraining the movement of the piston.

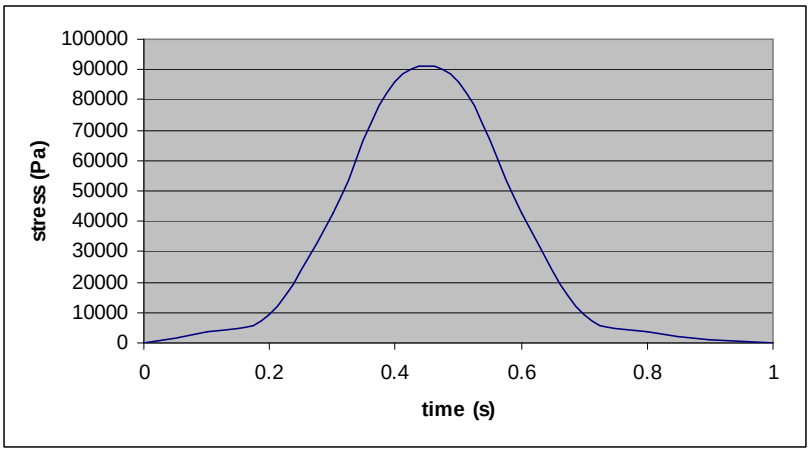

Figure 3.19 Vehicle-induced compressive impact stress on PZT stack. PZT stack locates at the mid-span point on the top of interior girder. A two-axle truck moves on bridge with speed 60mile/hour.

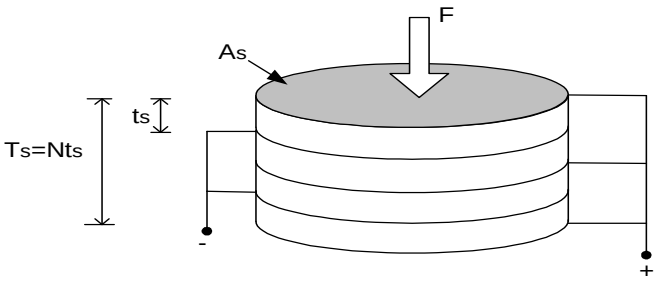

Figure 3.20 A multilayer stack under stress

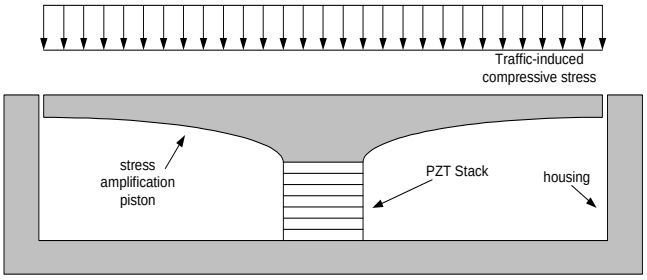

Figure 3.21 Stress amplification scheme

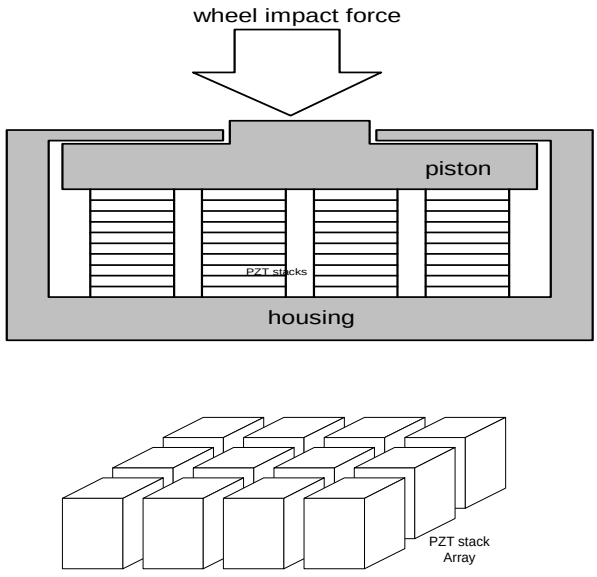

Figure 3.22 PZT stack array

3.3 Energy Storage Consideration

The generated power from a piezoelectric device has to be converted into a useful form. As just seen, although the output voltage from a piezoelectric transducer can be high, the output energy and frequency are quite low. Usually the generated charge passes a rectifier circuit, and then is stored in a capacitor bank. The capacitor is connected with a linear regulator (e.g. MAX666) [Maxim Integrated Products] which provides a specified stable voltage if the charge from the piezoelectric device can be generated continuously. This is the most direct and simple means of energy storing and discharging. In [Paradiso et al., 2001], the power harvested upon a single button push was stored and translated on the order of 0.5 mJ at 3 volts in 30 ms. However, charging a capacitor directly results in a substantial loss of the total available energy. More efficient means need to be developed. A self-powered digital signal processing system was tested and the generator subsystem and regulator architecture were discussed in [Amirtharajah et al., 1998]. [Shenck et al., 2001] introduced a forward-switching power-conditioning system which was more efficient for converting raw electric energy into a useful form. This scheme could be applied to the similar low-frequency piezoelectric source from bridge vibration.

3.4 Experimental Results

A simple experiment was conducted to verify the concepts of power scavenging described in the previous sections. A plastic beam (31.6cm×2.7cm×0.38cm) is used to generate vibration. The test setup is shown in Figure 3.23. The test sample is a single-layer PZT sheet (6.3cm×3.1cm×0.02cm). The PZT sheet is attached to a plastic beam. The plastic beam vibrates under its natural frequency (around 8 Hz). The output voltage

from electrodes on the PZT sheet was observed in an oscillograph. This is a validation testing for the patch-type generator. The output of PZT sheet subjected to mechanical vibration is measured, and the strain on the PZT sheet is also obtained from the strain gauge. The estimated values are calculated based on the strain value by applying the equations introduced in section 3.2.2. So the experimental results are compared to the estimated values. Moreover, various load resistances are connected to the patch generator, and the generated power is compared to the estimated values which are calculated by equation 3.5.

As shown in Figure 3.23, the single PZT sheet was attached close to the fixed end of the plastic beam, and a strain gauge was also installed at the same location of the plastic beam. The free end of the plastic beam was pushed to deflect 4cm then released. When the free end was pushed down to deflect 4cm, the strain value obtained from the strain gauge was 103 micro strain. Results show that the output is a periodic signal with frequency around 8 Hz which is close to the natural frequency of the plastic beam. With the effect of mechanical damping, the amplitude of the output signal decreased to zero after 5 seconds. The maximum peak-to-peak open voltage was measured to be around 25 volts. This is close to the estimated open voltage 30 volts, which is calculated based on the strain value obtained from the strain gauge. The power generation from the patch-type generator is about 210μW (302μW, estimated value). The peak power output under various load resistances is shown in Figure 3.24.

The experimental results show good agreement with the estimated values, and the patch-type generator performed properly as expected, and a remarkable amount of raw power is obtained from mechanical vibration.

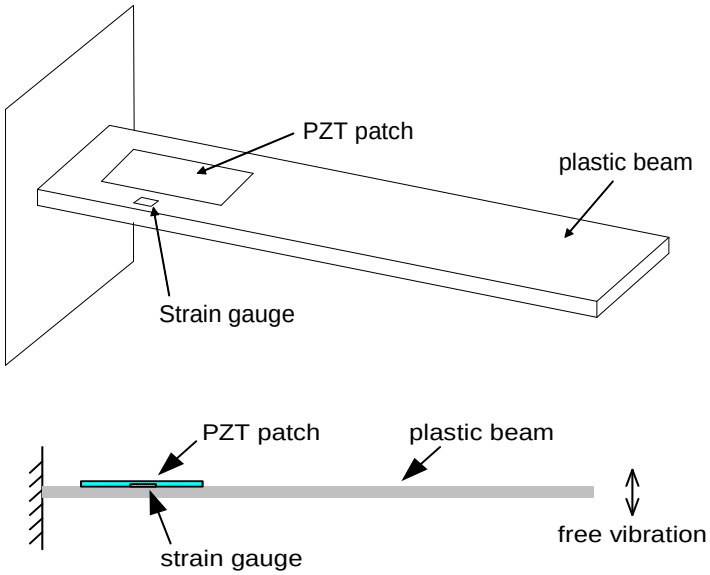

Figure 3.23 Parasitic patch on a free vibration beam

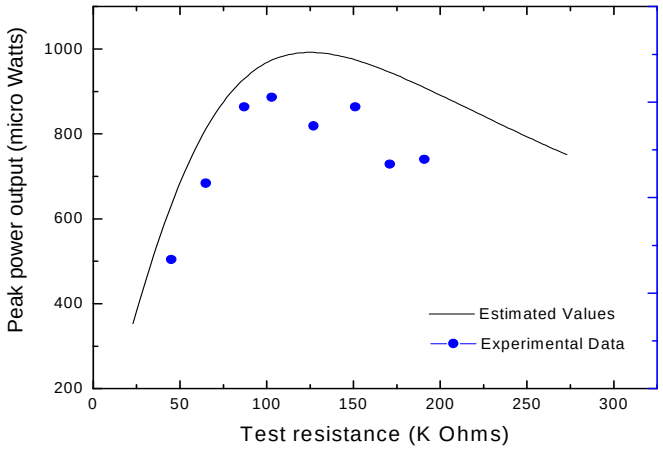

Figure 3.24 Experimental and estimated peak power output under different test resistance load

3.5 Comparison to other forms of available energy

Solar radiation is an attractive source for energy scavenging as its technology is well developed. A highway bridge has large amounts of surface exposed to sun light. No doubt that the solar energy collection transducer can provide abundant electric power on a sunny day. The available energy is decreased to roughly one hundredth of that on a cloudy day, and to one thousandth for indoor lighting conditions. When solar cells are placed on bridges, they are not always exposed directly to the sun even on sunny days. At locations of interior girders, the illumination is quite low and it is similar to indoor lighting conditions.

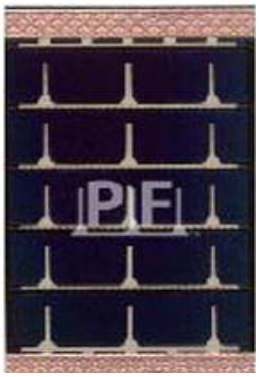

Figure 3.25 Solar panel

Many types of solar cells have been fabricated and studied. New solar cells have efficiency as high as 30%. Reference [Lee et al., 1995] introduces a miniaturized high-voltage solar array (100 cells in 1 cm^2) and it was utilized as a power supply for MEMS. SmartDust [Warneke et al., 2002] was designed to be powered by a SOI solar cell array which could harvest around 1 mW/mm^2 in full sunlight or 1 $\mu W/mm^2$ under bright indoor illumination with 10 to 12% efficiency.

Flexible solar panels are now commercially available. Figure 3.25 shows a 5cm ×3.8cm PowerFilm 3V 22mA solar panel supplied by Iowa Thin Film Technologies [Iowa Thin Film Technologies, Inc]. The power output is around 66 mW for direct sun (100%) and 0.1mW under low illumination conditions (0.1%). So the power generation density is in the range of 3.4mW/cm^2 to 5$\mu W/cm^2$.

Table 3.3 Power generation comparison

	sunny	cloudy	nighttime
Solar	3~10mW/cm^2	0.01~0.1mW/cm^2	0
Vibration	0.0004~1mW/cm^2	0.0004~1mW/cm^2	0.0004~1mW/cm^2

The piezoelectric based power generation density is in the range of 0.0004 to 1mW/cm^2. This is quite low compared to that of solar cells in sunny conditions. Table 3.3 shows the comparison. Even so, it is hard to say that solar power generation is the best choice to supply power for sensors in a bridge. The vibration-induced power generation has its competitive advantages. It is totally independent of climate and weather. At this point, solar cells are preferred in sunny conditions. Anytime the bridge is in use, piezoelectric transducers can generate power continuously both in daytime and nighttime. Moreover vibration-induced power generation is the most feasible means for powering embedded sensors. So a good idea would be to combine a vibration-based generator and solar cells together to power sensors in a bridge.

For a wireless sensor system, various operations consume different amount of power. Usually the operations include sensing/data processing, data transmission and system sleeping. The operation of sensing/data processing is to acquire the changes (e.g.: resistance change) of sensors, and process the raw data (e.g.: delete some unwanted or unimportant data). The operation of data transmission is to send out useful data as radio frequency signals, and the operation of system sleeping is to maintain the mode of sleeping, in which the system terminates other operations temporarily and waits for activation commands. Table 3.4 shows the power requirement for the operations of a

wireless sensor system. The estimation of power scavenging from both solar and bridge vibration is based on a 10 cm^2 generator and solar cell. In sunny days, the harvested power is sufficient for the operations of data transmission, sensing and data processing. In nighttime, the harvested power from bridge vibration is still enough for sensing, data processing and limited data transmission.

Table 3.4 Power obtained v.s. Power Demand

Power Obtained (based on 10 cm^2)			Power Demand [Amirtharajah et al, 1998], [Paradiso et al., 2001], [Arms et al., 2003], [Vittoz, 1994]		
	Daytime (sunny)	Nighttime	Sensing/data procesing	Data transmission	System sleeping
Solar	30~100mW	N/A	0.1~10mW	5~50mW	0.01~0.1mW
Vibration	0.004~10mW	0.004~10mW			
Sloar+Vibration	30~110mW	0.004~10mW			

Chapter 4

Resonant Beam-type Strain Sensor

Because traditional resistance strain gauges drift significantly over even short periods of time, they are not suitable for the purpose of “embedding”. A more stable strain sensor that is easily integrated with transceivers and system circuits is more desirable. In this chapter, a resonant beam strain sensor using standard CMOS MEMS technology [The MOSIS Service] is presented. Standard CMOS has been widely used to fabricate various sensors [Baltes, 1993], [Eyre et al., 1998]. The device in this chapter is a beam fixed at both ends for which the resonant frequency is determined by its axial stress. Changes in its axial stress give changes in its resonant frequency. The beams can be formed from metals or poly-silicon used in standard CMOS processing by etching thick field oxides away from underneath a beam.

The system of the vibrating beam strain sensor is shown in Figure 4.1. A current pulse generating circuit creates a positive pulse to charge up the capacitance with large charge Q_1 (to induce the beam vibration) and the discharge of the charge $Q_2 < Q_1$ (to leave a small amount of charge Q for detecting the beam vibration). The reason this scheme is chosen is explained in Section 4.3. The beam resonant frequency reflects the axial strain on the beam.

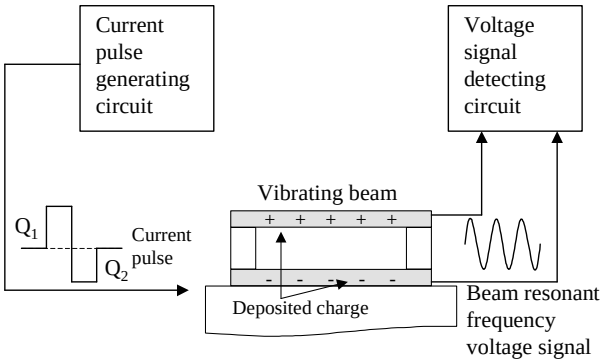

Figure 4.1 System for resonant beam strain sensor

The vibrating beam strain sensor can be embedded into a structure. For example, it can be mounted onto the steel rebar in a reinforced concrete structure, which is similar to the usage of vibrating wire spot-weldable strain gauge [Ace Instrument Co., Ltd.]. The axial strain in the vibrating beam is changed with the stress change in the steel rebar. So the strain of the rebar can be obtained by detecting the frequency change of the vibrating beam.

4.1 Beam Vibration Analysis

To study the beam vibration eigenvalues and eigenfunctions, the x and w axes are set up, as shown in Figure 4.2. The length of beam is l, the width is b, and the thickness is h.

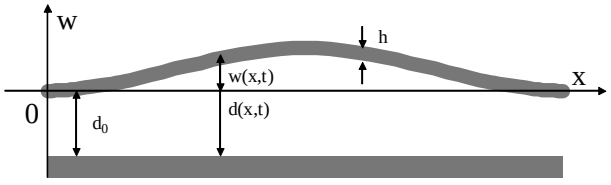

Figure 4.2 x and w axis set up for studying the beam vibration

In general, the differential equation of motion for beam structure is given by equation 4.1 [Sniegowski et al., 1999]:

$$\frac{\partial^2}{\partial x^2}\left(EI\frac{\partial^2 w(x,t)}{\partial x^2}\right)+\rho A\frac{\partial^2 w(x,t)}{\partial t^2}-P\frac{\partial^2 w(x,t)}{\partial x^2}=q(x,t) \tag{4.1}$$

where w(x,t) is the vertical deformation function of position x and time t. E is the Young's module, I is moment of inertia, ρ is density of the beam, A is the cross sectional area of the beam. P is the internal axial load applied on the beam and P=εEA, where ε is axial strain. q(x, t) is the external load on the beam. When there is neither axial nor perpendicular external load on the beam, the equation of motion can be written as equation 4.2.

$$\frac{\partial^2}{\partial x^2}\left(EI\frac{\partial^2 w(x,t)}{\partial x^2}\right)+\rho A\frac{\partial^2 w(x,t)}{\partial t^2}=0 \tag{4.2}$$

To obtain analytical solutions, separation of variables can be applied as shown in equation 4.3 [Shames et al., 1991].

$$w(x,t)=W(x)T(t) \tag{4.3}$$

Under the boundary conditions of both ends of the beam being clamped, the eigenfunctions can be solved as shown in equations 4.4 and 4.5.

$$T(t)=W_n\cos\left(\omega_n t+\alpha_n\right) \tag{4.4}$$

$$W_n(x)=\cosh\left(k_n x\right)-\cos\left(k_n x\right)+\frac{\cos\left(k_n l\right)-\cosh\left(k_n l\right)}{\sin\left(k_n l\right)-\sinh\left(k_n l\right)}\cdot\left(\sin\left(k_n x\right)-\sinh\left(k_n x\right)\right) \tag{4.5}$$

in which ω_n and k_n are:

$$\cos\left(k_n l\right)\cosh\left(k_n l\right)=1 \tag{4.6}$$

$$\omega_n^{\,2} = k_n^{\,4}\frac{EI}{\rho A} \qquad \text{n=1,2,3…} \tag{4.7}$$

When an axial force P is applied uniformly on the beam and the perpendicular external load on the beam is zero, the equation of motion of the beam can be written as equation 4.8.

$$\frac{\partial^2}{\partial x^2}\left(EI\frac{\partial^2 w}{\partial x^2}\right)+\rho A\frac{\partial^2 w}{\partial t^2}-P\frac{\partial^2 w}{\partial x^2}=0 \tag{4.8}$$

It is quite difficult to solve equation 4.8 analytically. One way to solve for the resonant frequency is the Rayleigh-Ritz method, and the solution has the form as shown in equation 4.9:

$$w(x,t)=W(x)\cos\left(\omega t+\alpha\right) \tag{4.9}$$

with W(x) as a trial function which satisfies the boundary conditions. Then $w(x,t)$ can be solved by this method, and the beam resonant frequency ω is a function of the strain applied on the beam. In this thesis, finite element code ANSYS is applied to simulate a vibrating beam under axial forces.

4.2 ANSYS Simulation Result

In this section, the resonant frequency variation with respect to the strain is presented. First, the situation when there is no pre-tension added on the beam was studied. Later, a pre-tensioned beam scheme is considered because the strain gauge should work under tension forces and compression forces. The simulation is done by using ANSYS [ANSYS, Inc., 1998].

4.2.1 Beam with no pre-tension

The schematic diagram of the vibrating MEMS beam is shown in Figure 4.3. The studied model is an fixed-end beam with length l of 100 micron, width of b=15 micron, and thickness of h=2 micron. The resonant frequencies of the beam structure under various situations of longitudinal axial stress are calculated in ANSYS. The composite material consists of SiO_2 and Metal layer (Aluminum). The Young's Modulus E and density ρ are given: for SiO2, ρ = 2200 Kg/m^3, E=57 to 85 GPa; for Aluminum, ρ = 2702 Kg/m^3, E=70 GPa [Gardner et al., 2001])

While applying a tensile stress σ along the beam, the strain in the beam is ε=σ/E. The resonant frequency change can be observed when the strain in the beam is changed. The ratio of the loaded resonant frequency and unloaded one, $f_r/f_{0,}$ is used to measure the resonant frequency change with respect to strain change. Figure 4.4 shows that the ratio f_r/f_0 has approximately a linear behavior with strain change.

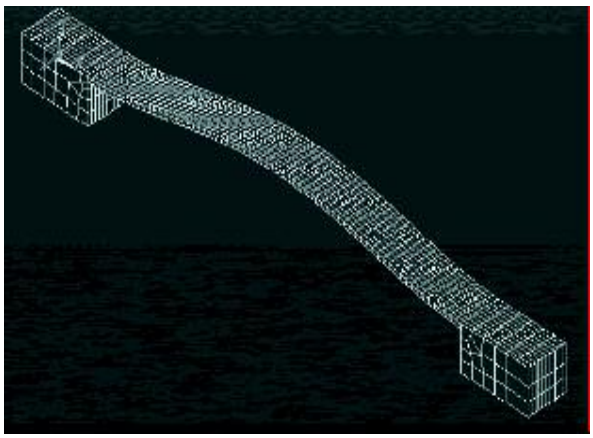

Figure 4.3 Schematic diagram of the vibrating MEMS beam

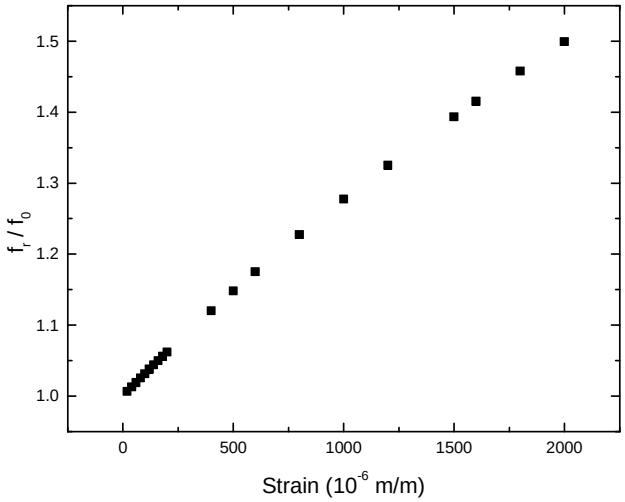

Figure 4.4 MEMS beam resonant frequency response with the strain change.

With zero longitudinal axial stress in the beam, its resonant frequency is 1133.08 KHz. Under an application of 500 micro strains in tension, the resonant frequency is shifted to 1300.83 KHz. The calculation result shows that the resonant beam is sensitive to the axial strain change as low as 1 micro strain with an increase of resonant frequency of about 0.5 KHz for 1 micro strain in tension.

4.2.2 Pre-tensioned MEMS Beam

A strain gauge is used to measure both tensile and compressive strain change in a structure. For the MEMS resonant beam strain gauge presented here, a small compressive stress will easily make the thin beam structure buckle. There have been studies and reported results on growing pre-stressed layers [Ferman, 1999]. MOS fabrication is also adopting the technology of growing pre-strained layers in MOS transistor fabrication to improve the performance and to look for new devices [Ernst et al., 2002].The making of pre-tensioned beams is not well developed, but it is possible.

For example, when the beam is pre-tensioned under 1000 micro strains, the initial resonant frequency f_0 will be 1447.33 KHz. If an external compressive force is applied on the strain gauge, let's say, 500 micro strains generated in compression, there is still 500 micro strains in tension in the beam. The resonant frequency is shifted to f_r =1300.83KHz comparing to1447.33KHz.

4.3 Capacitance Excitement of the Beam Vibration

To excite the beam vibration, a pulse of current is used to charge the capacitance plates, with a large charge Q_1. Then the Coulumb force on the beam bends the beam and excites the vibration. The current-pulse driven electrostatic actuators are examined in [Castañer et al., 2001].

The Coulumb force, q_0, per unit length on the bridge is given in equation 4.10:

$$q_0 = \frac{1}{2} \cdot \frac{Q^2}{\varepsilon_0 l^2 b} \tag{4.10}$$

Under a uniform force, q_0, per unit length perpendicular to the beam, the deformation equation of the resonant beam is:

$$w(x) = \frac{q_0 l^4}{8\pi^4 EI} \sum_{n=1}^{\infty} \frac{\left(1 - \cos\frac{2n\pi}{l}\right)}{n^4} \tag{4.11}$$

The mid point of the beam has the maximum deformation:

$$w\left(\frac{l}{2}\right) = \frac{q_0 l^4}{8\pi^4 EI} \sum_{n=1}^{\infty} \frac{\left(1 - \cos n\pi\right)}{n^4} \cong \frac{41 q_0 l^4}{162\pi^4 EI} \tag{4.12}$$

To be able to excite the beam, a charge Q1 has to be relatively large so the Coulumb force could give the beam enough deformation. Assuming the mid point

deflection is 0.1 micro meters, the required charge on the beam is about 8.4×10^{-13} Coulumbs based on equations 4.10 to 4.12. This is much smaller than the charge generated from a PZT patch described in section 3.2.2. The generated charge from the PZT patch is in the order of 10^{-6}:

$$Q=C_0U=8\times10^{-8}\text{Farads}\times32\text{volts}=2.6\times10^{-6}\text{Coulumbs} \quad (4.13)$$

So the harvested power from bridge vibration, as described in section 3, is sufficient to excite the beam considered here.

Since q(x,t) plays an important role in equation 4.1 which describe the motion of the beam, solution of the eigenvalues cannot be usually done in closed-form. Also, the resonant frequency of the beam is also charge dependant, something that leads to difficulty for calibration.

The scheme considered to solve this problem here is to use a positive current pulse, followed by a negative pulse. Therefore, the capacitance is charged up with a large Q_1 to excite the beam vibration. Then the capacitance is discharged by a slightly smaller charge, Q_2. Only a small amount of charge, Q_1-Q_2, is left on the capacitance. Since the charge is small, the remaining Coulumb force on the beam is negligible in the equation of motion. Equations 4.2 and 4.8 can be used to describe the motion of the beam without and with axial force.

4.4 Capacitance Detection of the Beam Resonant Frequency

The beam resonant frequency can be determined by measuring the output AC voltage frequency. The output voltage is related to the capacitance between the vibrating

beam and bottom plate. To calculate the capacitance, as shown in Figure 4.2, first look at the infinitesimally small capacitance, which is expressed by equation 4.14,

$$\Delta C(x,t) = \frac{\varepsilon_0 b}{d(x,t)} dx \tag{4.14}$$

in which ε_0=8.85×10^{-12} farads/m, the permittivity of vacuum,

and

$$d(x,t) = w(x,t) + d_0 \tag{4.15}$$

For $w(x,t) << d_0$,

$$\Delta C(x,t) = \frac{\varepsilon_0 b}{d_0} \cdot \frac{1}{1 + \frac{w(x,t)}{d_0}} \cong \frac{\varepsilon_0 b}{d_0} \cdot \left(1 - \frac{w(x,t)}{d_0}\right) \tag{4.16}$$

Then the capacitance between the two plates can be expressed as equation 4.17:

$$C(t) = \int_0^l \Delta C(x,t) = \frac{\varepsilon_0 b}{d_0} \cdot \int_0^l \left(1 - \frac{w(x,t)}{d_0}\right) dx \tag{4.17}$$

Equation 4.17 can be rewritten as:

$$C(t) = C_0 \left(1 - \frac{1}{d_0 l} \int_0^l w(x,t) dx\right) \tag{4.18}$$

in which C_0 is the capacitance of the beam with no deformation:

$$C_0 = \frac{\varepsilon_0 b l}{d_0} \tag{4.19}$$

where d_0 is the gap distance between the vibrating beam and the substrate.

The current pulse generation circuit charges up the capacitance with fixed charge quantantity Q, then the voltage between the two plates can be expressed as equation 4.19.

$$V(t) = \frac{Q}{C(t)} \tag{4.20}$$

For $w(x,t) << d_0$, and with $V_0 = Q / C_0$,

$$V(t) = \frac{V_0}{\left(1 - \frac{1}{d_0 l}\int_0^l w(x,t)dx\right)} \tag{4.21}$$

Normally, when the beam is excited to vibrate, many modes exist. When the uniformly distributed force is added to excite the beam vibration, the dominant mode is the fundamental mode. To simplify the analysis, only the first mode is considered in this case. The capacitance and voltage are expressed by equations 4.18 and 4.21.

As shown in equation 4.21, V(t) has the same frequency as w(x,t), so the small AC voltage signal has the same frequency as the resonant frequency of the beam. Therefore, by detecting the AC voltage frequency, the strain on the beam can be obtained.

4.5 Temperature Compensation

Temperature compensation is a significant issue for a strain sensor. The ambient temperature effect can be compensated by measuring the temperature with a strain-insensitive resonant beam. The strain-insensitive beam can be a cantilevered beam with the same width as the strain-sensitive beam, but it is detached from one support so that its vibration is not affected by the strain, as shown in Figure 4.5.

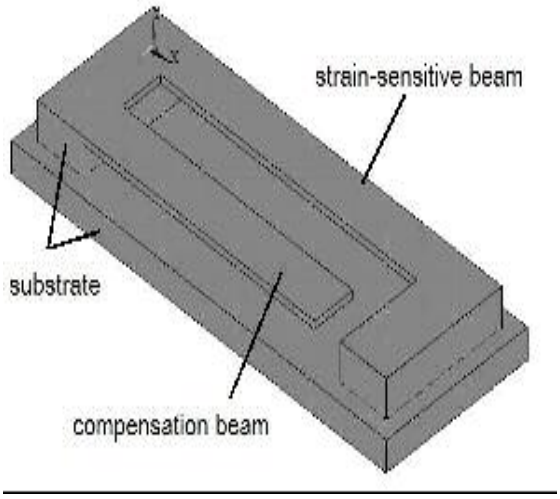

Figure 4.5 Schematic diagram of compensation beam structure

The signal out from the compensation cantilever beam can be compared to its calibration values so as to obtain the temperature effect. So the signal out from the fix-end resonant beam can be adjusted.

In this chapter, a scheme of using resonant beam to detecting the strain on the beam has been demonstrated. The theoretical analysis is given along with the ANSYS simulation results. Also, a temperature compensation scheme is provided. The results show that detection of the AC voltage frequency can be used to detect strain.

Chapter 5

Measurement of Propagation Attenuation through Concrete

Embedded sensors are designed to be mounted onto steel rebars of a reinforced concrete structure, and the strain information can be sent out via a radio frequency transceiver module as described in Chapter 2. In this way, the reliance of wires for communicating between sensors and central units can be eliminated. Chapter 3 shows that the harvested power from bridge vibration and solar cells can provide sufficient power supply for the operations of the embedded sensor system. However, an important issue has to be considered: signal attenuation in concrete. The higher the attenuation is, the more power a transceiver module consumes in order to ensure that the received signal strength can be sustained in a detectable level. The investigation on the signal attenuation in concrete provides a reference for transceiver design and embedded sensors placement.

In this chapter, a theoretical study is presented and validates experimental measurements. The measurements are taken at the 900 MHz radio frequency range which is an unlicensed Industrial, Scientific, Medical (ISM) radio band widely used in civil applications.

5.1 Electromagnetic Wave Propagation

5.1.1 Reflection and Transmission Coefficient

Consider a uniform plane wave impinging from medium 1 (ε_1, μ_1) to medium 2 (ε_2, μ_2). ε, μ are the electric permittivity and magnetic permittivity of the materials. At the

boundary of two different materials, part of the incident energy is reflected back into medium 1 and the rest of the energy is transmitted into medium 2. The normal of the boundary and the incident wave propagation vector form the *plane of incidence*, as shown in Figure 5.1 The angle of incidence is denoted as θ_1, and the angle of transmission is denoted as θ_2. θ_2 can be obtained from Snell's law:

$$\theta_2 = \sin^{-1}\left(\sqrt{\frac{\mu_1\varepsilon_1}{\mu_2\varepsilon_2}}\sin\theta_1\right) \tag{5.1}$$

Air and construction material such as concrete, wood etc. are low conducting medium, and their relative magnetic permittivity are approximately equal to 1.

$$\mu_1 = \mu_2 = \mu_0 \tag{5.2}$$

μ_0 is the magnetic permittivity of free space and equal to $4\pi \times 10^{-7}$ Henry/meter.

So equation 5.1 can be written as:

$$\theta_2 = \sin^{-1}\left(\sqrt{\frac{\varepsilon_1}{\varepsilon_2}}\sin\theta_1\right) \tag{5.3}$$

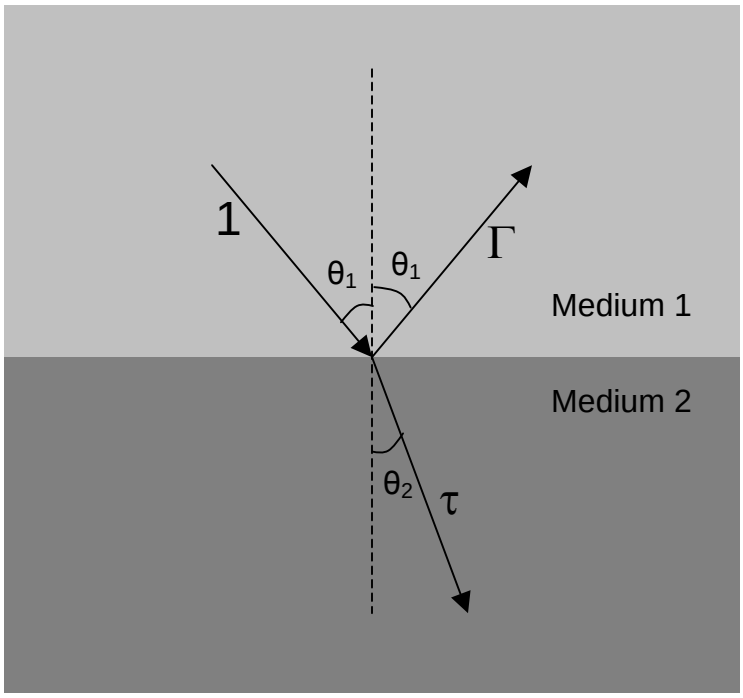

Figure 5.1 Electromagnetic wave propagates from medium1 to medium 2

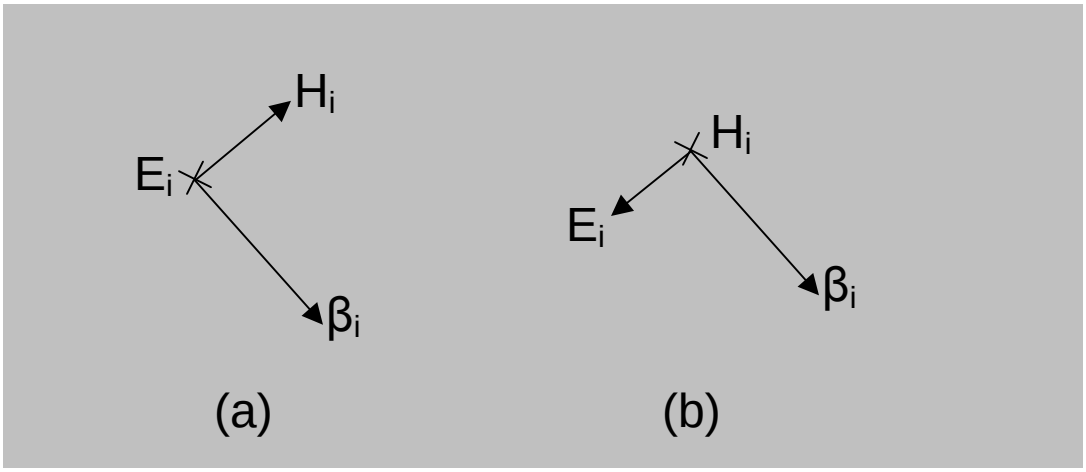

Figure 5. 2 Schematic drawings of TE and TM waves

Figure 5.2 shows two types of electromagnetic waves with same propagation vector. E_i, H_i, β_i represent electric field, magnetic field and propagation vector, respectively. Figure 5.2(a) shows that the electric field vector is perpendicular to the plane of incidence and this type of wave is called Transverse Electric (TE) wave. Figure

5.2(b) shows that the electric field vector is parallel to the plane of incidence and this type of wave is called Transverse Magnetic (TM) wave.

When a handheld device is designed to communicate with embedded sensor, it is necessary to know how much energy of the signal is transmitted into concrete and how much can be received by sensors. So the reflection coefficient and transmission coefficient are considered.

The reflection coefficient of TE wave is [Rao, 1999]:

$$\Gamma_{TE} = \frac{\sqrt{\varepsilon_1}\cos\theta_1 - \sqrt{\varepsilon_2}\cos\theta_2}{\sqrt{\varepsilon_1}\cos\theta_1 + \sqrt{\varepsilon_2}\cos\theta_2} \tag{5.4}$$

The transmission coefficient of TE wave is [Rao, 1999]:

$$\tau_{TE} = \frac{2\sqrt{\varepsilon_1}\cos\theta_1}{\sqrt{\varepsilon_1}\cos\theta_1 + \sqrt{\varepsilon_2}\cos\theta_2} \tag{5.5}$$

The reflection coefficient of TM wave is [Rao, 1999]:

$$\Gamma_{TM} = \frac{\sqrt{\varepsilon_1}\cos\theta_2 - \sqrt{\varepsilon_2}\cos\theta_1}{\sqrt{\varepsilon_1}\cos\theta_{21} + \sqrt{\varepsilon_2}\cos\theta_1} \tag{5.6}$$

The transmission coefficient of TM wave is [Rao, 1999]:

$$\tau_{TM} = \frac{2\sqrt{\varepsilon_1}\cos\theta_1}{\sqrt{\varepsilon_1}\cos\theta_2 + \sqrt{\varepsilon_2}\cos\theta_1} \tag{5.7}$$

When a normal wave impinges to the interface (θ_1=0), the reflection and transmission coefficient can be written:

$$\Gamma = \frac{\sqrt{\varepsilon_1} - \sqrt{\varepsilon_2}}{\sqrt{\varepsilon_1} + \sqrt{\varepsilon_2}} \tag{5.8}$$

$$\tau = \frac{2\sqrt{\varepsilon_1}}{\sqrt{\varepsilon_1} + \sqrt{\varepsilon_2}} \tag{5.9}$$

τ=1 means all wave energy is transmitted from medium 1 to medium 2, and τ=0 means all wave energy is reflected at the interface.

5.1.2 Penetration Depth

Consider a plane wave with electric field of the form:

$$\overline{E} = E_0 e^{(-jk^*\overline{\rho} + j2\pi ft)} \tag{5.10}$$

where k^* is complex wave number in direction $\overline{\rho}$, and $\overline{\rho}$ is position vector. k^* has real part k_r and imaginary part k_i ($k^* = k_r - jk_i$). The plane wave can be written:

$$\overline{E} = E_0 e^{(-j(k_r - jk_i)\overline{\rho} + j2\pi ft)} = E_0 e^{-k_i\overline{\rho}} e^{(-jk_r\overline{\rho} + j2\pi ft)} \tag{5.11}$$

It shows that the magnitude of the wave is changed to $E_0 e^{-k_i\overline{\rho}}$. This attenuation is due to the wave propagation in dielectric material in direction $\overline{\rho}$. Attenuation factor can be written as:

$$\gamma = 20\log(e^{k_i}) \tag{5.12}$$

The magnitude of the wave can be written in terms of propagation depth d_{pg}:

$$E_{mag} = E_0 e^{-k_i d_{pg}\overline{\rho}} \tag{5.13}$$

For dielectric material with low conductivity, k_i can be written in terms of ε_r' and ε_r" which are the real and imaginary parts of the relative dielectric constant:

$$k_i = \pi f\left(\sqrt{\frac{\varepsilon_0\mu_0}{\varepsilon_r'}}\varepsilon_r''\right) \tag{5.14}$$

The relative complex dielectric constant is defined as:

$$\varepsilon_r = \varepsilon_r' + j\varepsilon_r'' \tag{5.15}$$

The real part ε_r' is related to the energy stored in dielectric material and the imaginary part ε_r'' is related to the energy dissipated.

Penetration depth is defined as the distance at which wave field strength falls to 1/e (36.8%) of its initial value:

$$d_p = \frac{1}{k_i} = \frac{\sqrt{\varepsilon_r'}}{\pi f \sqrt{\varepsilon_0 \mu_0}\, \varepsilon_r''} \tag{5.16}$$

f is the frequency in Hz of incident wave.

5.2 Dielectric Constant of Concrete

The complex dielectric constant of concrete is dependent on the frequency in low radio frequencies range, and this dependency is significantly reduced in the microwave frequencies. This is shown in Figure 5.3. In [Loulizi, 2001], concrete slabs with different mix constituents were tested to obtain the complex dielectric constant of concrete in the frequency range of 0.5 to 1.0GHz. Reference [Rhim et al., 1998] also studied the variation of dielectric constant of concrete with different moisture content in the frequency range of 0.1 to 20GHz. With the knowledge of dielectric constant, the transmission coefficient and penetration depth can be obtained from equations 5.4 to 5.7 and 5.16.

Figure 5.3 shows that the complex dielectric constant of concrete is about 9+2j. Substitute ε_r'=9, ε_r''=2 and f=917.5MHz into equation 5.15, the penetration depth is:

$$d_p = \frac{\sqrt{9}}{3.14 \times 917.5 \times 10^6 \times \sqrt{8.85 \times 10^{-12} \times 4 \times 3.14 \times 10^{-7} \times 2}} = 15.6cm.$$

This means that the power of a signal (917.5MHz) falls to 36.8% of its initial value when it penetrates a depth of 15.6cm in concrete.

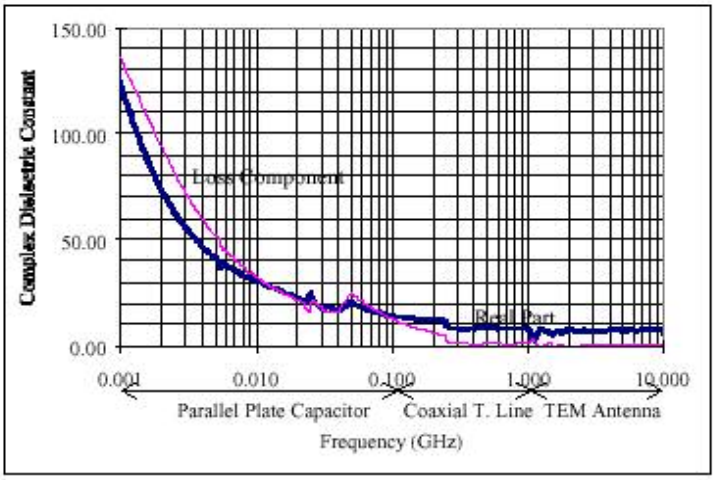

Figure 5.3 [Loulizi, 2001] Concrete dielectric constants vs. frequency

5.3 Experimental Set-up and Results

Figure 5.4 shows the experimental set-up. Two antennas are placed facing each other directly, and the samples are placed between them. Network analyzer is used to take the measurement of the two antennas. Antennas are connected to the ports of the network analyzer. The diffraction effects at sample edges have been minimized by increasing sample area and by making antennas axially perpendicular to sample plane. The S_{12} reading (in dB) of the network analyzer gives the ratio of the energy received by the receiving antenna and the energy sent by the transmitting one, $S_{12}=20\log_{10}(E_{OUT}/E_{IN})$.

The Two helical antennas are designed with the working range of 0.8 GHz to 1.1 GHz and one functions as the transmitting antenna and the other as the receiving one. Helical antenna is considered because of its high directivity when it is operating in the axial mode [Balanis, 1982] as shown in Figure 5.5. Total length L=30cm, diameter D=10cm, spacing s=7.5cm and total turns N=4. Helical antenna is formed by screwing a conducting wire. The radiation characteristics of antenna can be changed by controlling the dimensions. Axial mode is the most practical operation of helical antenna. In this mode, the majority of radiation intensity is along the helix axis. In order to excite this mode, the ratio $\pi D/\lambda$ must be between *3/4* and *4/3*. Usually the helical antenna is used with a ground plane whose diameter is at least $\lambda/2$. For 917MHz wave, $\lambda/2$ is equal to 16.4cm. A 20cm×20cm copper plate is used in the experiment.

The nominal impedance of the helical antenna in axial mode is in the range of 100 to 200 Ohms. A thin metal strip is attached to the wire close to the feed point, and the antenna impedance is then adjusted to 50 Ohms by changing the size of metal strip in order to match the impedance of transmission lines.

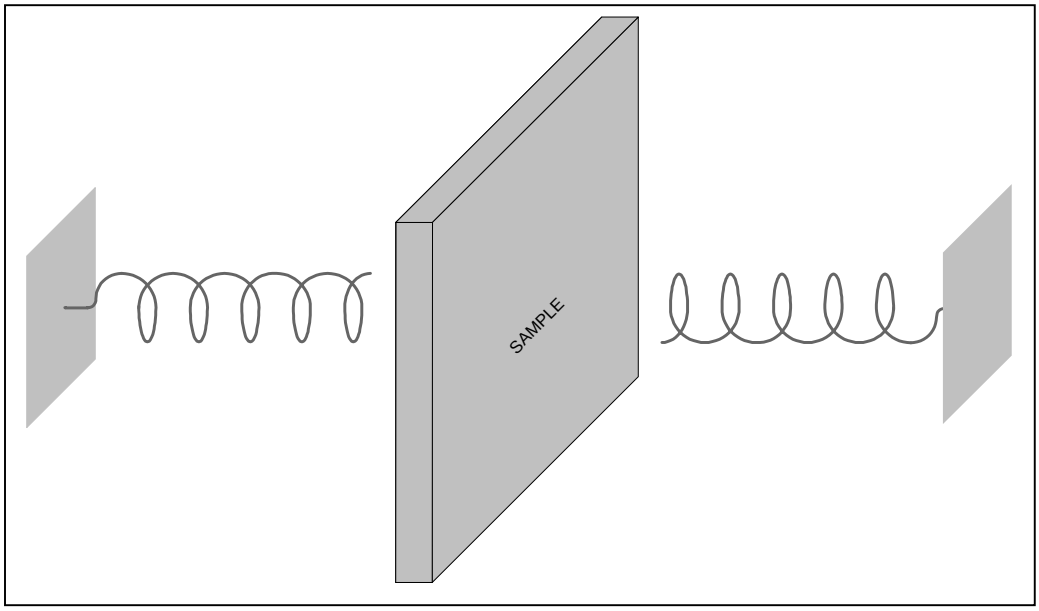

Figure 5.4 Schematic drawing of experiment setup

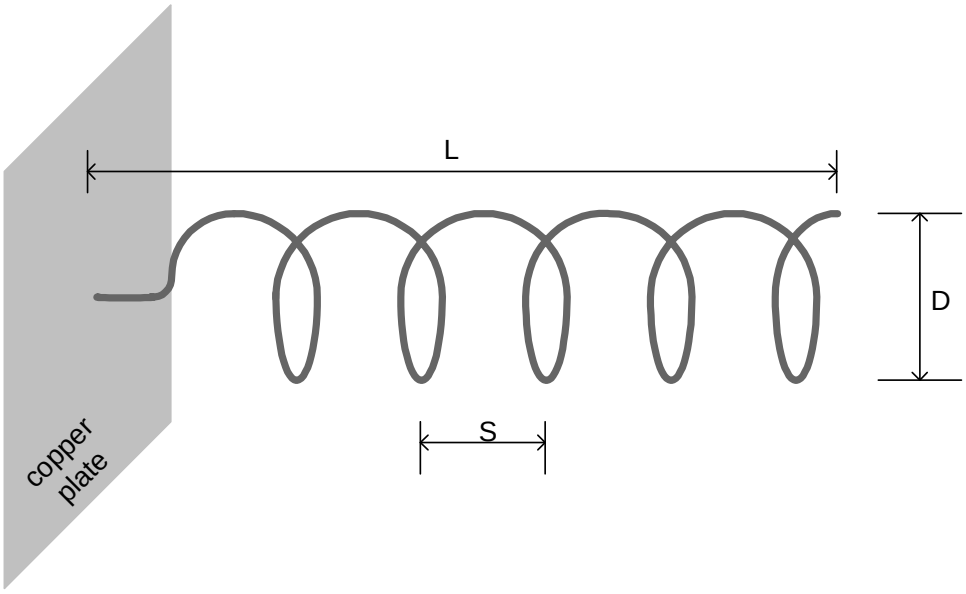

Figure 5.5 Schematic drawing of helical antenna

In order to compare the influence of concrete with other materials, the measurements were taken under four situations. (a) There is no blocking between the two

antennas; (b) Wall board is inserted between the two antennas; (c) Concrete slab with 4.5 inch thickness is inserted between the two antennas. (d) Metal plate is inserted between the two antennas. The output of the network analyzer gives the S_{12} reading (in dB) with respect to wave frequency, as shown in Figure 5.6. X-axis denotes the frequency that varies from 0.5 to 1.5 GHz. Since the antennas are designed to operate in 0.8 to 1.1 GHz, Figure 5.6(a) shows that the antenna has less noise in this range. 917.5MHz is marked as the tracking point and results of measurement taken at this point are presented in Table 5.1.

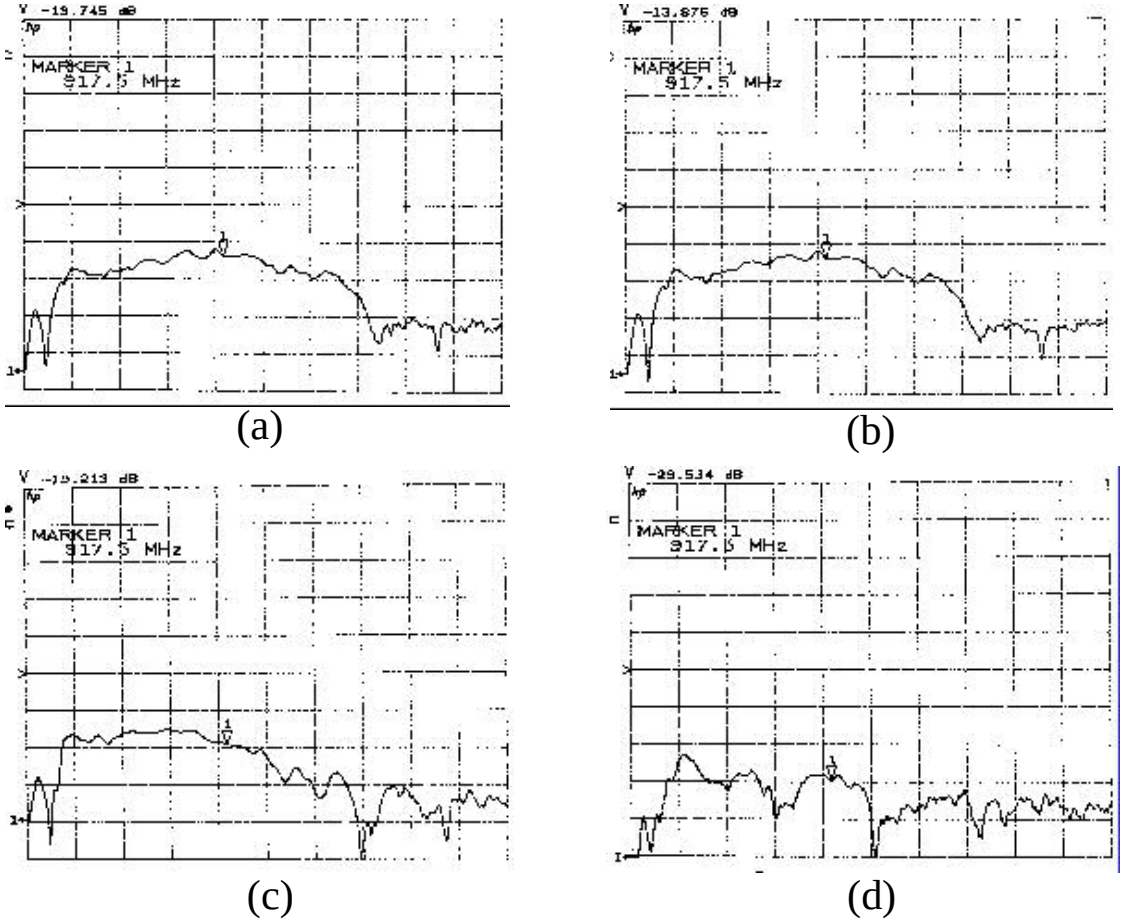

Figure 5.6 Transmitting of RF energy through different material. (a) Open space. (b) Wood wall board. (c) Concrete slab. (d) Metal plate. For all four plots, x-axis frequency vary from 0.5 to 1.5 GHz, with 50 MHz per grid. y-axis is the $20\log_{10}(E_{OUT}/E_{IN})$, with 10 dB per grid.

Table 5.1 Attenuation taken at 917.5MHz

Tested Sample	Propagation Attenuation
(a) Open Space	-14dB
(b) Wood Wall Board	-14dB
(c) Concrete Slab	-19dB
(d) Metal Plate	-30dB

Results show that the wood wall board barely had any influence on the measurement. With the concrete slab, the reading dropped about 5 to 6 dB

($E_{OUT} / E_{IN} = 10^{(S_{21}/20)} = 56.2\%\ to\ 50.1\%$) at 917.5 MHz. That means there is about 50% power lost. To get an idea about energy level of the scattering field, a metal plate was inserted between the two antennas to block the direct transmission between them. The reading dropped about 30 dB ($E_{OUT} / E_{IN} = 3.2\%$), which is 11 dB more than the loss due to the concrete slab.

A 5 to 6 dB power loss due to a concrete slab with 4.5 inch (11.4cm) thickness was found in the experiment. The experimental results also show that the signal attenuation due to wood wall board is small enough to be neglected. Equation 5.15 shows that every time the signal (917.5MHz) penetrates a depth of 15.6cm in concrete, the power of the signal fall to 36.8%. So if the signal penetrates a depth of 4.5 inch (11.4cm), the power falls to 48.2% ($e^{-0.73}$, from equation 5.13) of its initial value. This is very close to the experimental results (50.1% to 56.2%).

Chapter 6

Summary and Conclusion

In this thesis, an embedded sensor system for structural health monitoring is described. The sensor system collects structural information by detecting embedded strain sensors. A power scavenging device is employed to harvest energy from highway bridge vibration for the power demand of the sensor system. The structural information is sent back to a handheld monitor wirelessly. This thesis concentrates on three topics:

6.1 power scavenging from highway bridge vibration

Scavenging energy from the ambient is an attractive means to power sensors in structures. This eliminates the dependence of batteries and allows the sensors to be tetherless. Power scavenging from traffic-induced vibration of highway bridge vibration is investigated and PZT (lead zirconate titanate) material is studied as the major piezoelectric element for power generation. Three mechanisms (Patch, cantilever beam and stacks) are described that are suitable for sensors to scavenge mechanical energy at different locations. The PZT patches can also be used to sense the strain changes in bridge girders. The harvested power is relatively low due to the low strain changes. The generated power level is about $0.5\mu W/cm^2$. Cantilever beam device is design to sense bridge vibration and generates high strain. The power generation from this mechanism is about $20\mu W/cm^2$ and its dimension can be optimized in order to maximize the generated power in different vibration environments. PZT stacks and stack arrays have the biggest potential ($1mW/cm^2$) of the three schemes investigated. By applying the stress

amplification scheme, a multilayer stack generates around 1mW power under traffic-induced vertical compressive stress at the top of girders. A stack array scheme is designed to be placed in pavement and it makes use of the wheel impact force on pavement. All calculations are based on the vibration data of a single span girder bridge using the finite element code ANSYS. The dynamic performance is studied by simulating trucks moving across the bridge. The results show that the power generation density of 0.0004mW/cm^2 (for patches) to 1mW/cm^2 (for stacks) can be achieved. Solar power harvested in solar cells is 3 to 10mW/cm^2 in sunny day, and 0.01 to 0.1mW/ cm^2 in cloudy day. Solar cells have the limitation in nighttime and low light conditions. However the vibration-induced power generation is independent of climate and weather. So combing vibration-induced power generator and solar cells together is an effective way to provide power supply for the operation an embedded sensor system, including sensing, data processing and signal transmission.

6.2 Embedded MEMS beam-type strain sensor

A scheme of using resonant beam to detect the axial strain of the MEMS beam is demonstrated. The resonant frequency of the vibrating beam is determined by its axial stress. This allows for detection of under one micro strain (10^{-6} m/m) change in a 100 micron long beam both for compression and tension. The strain on the beam can be sampled remotely by observing the resonant frequency of beam while compensation for such factors as temperature change can be performed. The theoretical analysis is given along with the ANSYS simulation results and the capacitance excitement and detection

technologies are provided. The results show that detection of the AC voltage frequency provides beam strain information.

6.3 Propagation Attenuation through Concrete at 900 MHz

The propagation of radio frequency signal through concrete at 900 MHz range is discussed. Measurements are taken to determine the radio frequency energy attenuation while transmitting through a 4.5 inch concrete slab, a wood wallboard and a metal sheet. The results show that the wood wallboard has very little effect on signal propagation. A 5 to 6 dB loss due to the concrete slab with 4.5 inch thickness is found. The experimental results have a good agreement to the theoretical calculations. The theoretical study and experimental measurement provide a reference for determining embedded depth of sensors in concrete and designing the transceiver module of an embedded sensor system.

References

Ace Instrument Co., Ltd., http://my.ecplaza.net/aceins/3.asp

Amirtharajah R and Chandrakasan A.P., 1998, "Self-Powered Signal Processing Using Vibration-Based Power Generation," IEEE Journal of Solid-State Circuits, Vol. 33, No. 5, pp. 687-695, May

ANSYS, Inc., 1998, Tenth Edition ANSYS Manuals Release 5.5, September

Arms S.W. and Townsend C. P., 2003, "Wireless Strain Measurement Systems –Applications & Solutions," Presented at NSF-ESF Joint Conference on Structural Health Monitoring, Strasbourg, France, October

Balanis C. A., 1982, Antenna Theory Analysis and Design, pp. 386, Harper & Row Publishers

Baltes H. P., 1993, "CMOS as sensor technology," Sensors and Actuaters, A37-38, pp.51-56, June-August

Castañer L., Pons J., Nadal-Guardia R. and Rodríguez A., 2001, "Analysis of the extended operation range of electrostatic actuators by current-pulse drive," Sensors and Actuators A 90, pp.181-190

El-hami M., Glynne-Jones P., White N. M., Hill M., Beeby S., James E., Brown A. D., Ross J. N., 2001, "Design and fabrication of a new vibration-based electromechanical power generator," Sensors and Actuators Vol. 92, pp.335-342

Ernst T., Hartmann J.-M., Loup V., Ducroquet F., Dollfus P., Guegan G., Lafond D., Holliger P., Toffoli A., and Deleonibus S., 2002, "Fabrication of a Novel Strained SiGe: C-Channel Planar 55nm nMOSFET for High-Perfomance CMOS," 2002 Symposium on VLSI Technol., Hilton Hawaiian Village, Honolulu, HI, June 11-15

Eyre B. and Miller L., 1998, "MEMS Magnetic Sensor in Standard CMOS," Science Closure and Enabling Technologies for Constellation Class Missions, edited by V. Angelopoulos and P. V. Panetta, pp. 99-102, UC Berkeley, Calif.

Ferman M. A. 1999, "Silicon-Based Heterostructures: Strained-Layer Growth by Molecular Beam Epitaxy," Cryst. Res. Technol. Vol. 34, pp. 583-595

Friedman D., Heinreich H., and Duan D.W., 1997, "A low-power CMOS integrated circuit for field-powered radio frequency identification tags," ISSCC Dig. Tech. Papers, Feb. 1997, pp. 294-295

Gardner J. W., Varadan V. K., Osama A. O., 2001, Microsensors MEMS and Smart Devices. John Wiley & Sons Ltd, Chichester, England

Glosch H., Ashauer M., Pfeiffer U., Lang W., 1999, "A thermoelectric converter for energy supply," Sensors and Actuators Vol. 74, pp.246-250

Glynne-Jones P., Beeby S.P. and White N.M., 2001, "Towards a piezoelectric vibration-powered microgenerator," IEE Proc. –Sci. Meas. Technol., Vol. 148, No. 2, pp.68-72, March

Honcharenko W., Bertoni H. L., Dailing J. L., Qian J., and Yee H. D., 1992, "Mechanisms Governing UHF Propagation on Single Floors in Modern Office Buildings," IEEE Transaction on Vehicular Technology, Vol. 41, No. 4, November

Honcharenko W., Bertoni H. L., and Dailing J., 1993, "Mechanism Governing Propagation Between Different Floors in Buildings," IEEE Transaction on Antennas and Propagation, Vol. 41, No. 6, June

Iowa Thin Film Technologies, Inc., http://www.iowathinfilm.com/

Jung K., Bredow J. W., Joshi S. P., 1999, "Electromagnetically coupled embedded sensors," Proceedings of SPIE Vol. 3674, Industrial and Commercial Applications of Smart Structures Technologies

Kendall C. J., 1998, "Parasitic Power Collection in Shoe Mounted Devices," Thesis of Bachelor Degree, Massachusetts Institute of Technology, June

Kovács Ádám and Vízváry Zsolt, 2001, "Structural parameter sensitivity analysis of cantilever- and bridge-type accelerometers," Sensors and Actuators A 89 (2001) 197-205

Lafortune J. F. and Lecours M., 1990, "Measurement and Modeling of Propagation Losses in a Building at 900 MHz," IEEE Transaction on Vehicular Technology, Vol. 39, No. 2, May

Lawton M. C. and McGeehan J. P., 1994, "The Application of a Deterministic Ray Launching Algorithm for the Prediction of Radio Channel Characteristics in Small-Cell Environments," IEEE Transaction on Vehicular Technology, Vol. 43, No. 4, November

Lee J. B., Chen Z., Allen M. G., Rohatgi A. and Arya R., 1995, "A Miniaturized High-Voltage Solar Cell Array as an Electrostatic MEMS Power Supply," IEEE Journal of MEMES, Vol. 4, No. 3, September

Loulizi Amara, 2001, "Development of Ground Penetrating Radar Signal Modeling and Implementation for Transportation Infrastructure," Ph.D. Dissertation, Virginia Polytechnic Institute and State University, February

Lynch J. P., Law K. H., Straser E. G., Kiremidjian A. S. and Kenny T. W., 2000, "The Development of a Wireless Modular Health Monitoring System for Civil Structures,"

Proceedings of the MCEER Mitigation of Earthquake Disaster by Advanced Technologies (MEDAT-2) Workshop, Las Vegas, NV, USA, November

MathWorks, Inc., http://www.mathworks.com

Maxim Integrated Products, http://www.maxim-ic.com/quick_view2.cfm/qv_pk/1330

Meninger S.,Mur-Miranda J.O., Amirtharajah R, Chandrakasan A.P., Lang J.H., 2001, "Vibration-to-Electric Energy Conversion," ISPLED99, pp. 48-53

MicroStrain, Inc., http://www.microstrain.com/SG-Link.htm

Morgan Electro Ceramics, http://www.morganelectroceramics.com/

Morgan Electro Ceramics, 2000, "Piezoelectricity High Voltage Generators," Technical Publication TP-219

Paradiso J. A. and Feldmeier M, 2001, "A Compact, Wireless, Self-Powered Pushbutton Controller," UBICOMP Conference Proceedings, Atlanta GA, Sept. 2001, Springer-Verlag Berlin Heidelberg,

Pfeifer K. B., Leming S. K., and Rumpf A. N., 2001, "Embedded Self-Powered MicroSensors for Monitoring the Surety of Critical Buildings and Infrastructures," Sandia National Laboratories, SANDIA REPORT, SAND2001-3619, Unlimited Release, Printed November

Piezo Systems, Inc., Piezo Generator/Sensor Kit Manual, 186 Massachusetts Ave. Cambridge, MA 02139 USA

Rao Nannapaneni N., 1999, "Elements of Engineering Electromagnetics," Ftfth Edition, PRENTICE HALL, Upper Saddle River, NJ 07458

Rhim H. C. and Büyüköztürk R., 1998, "Electromagnetic Properties of Concrete at Microwave Frequency Range," ACI Material Journal, pp. 262-271, May-June

Seidel S. Y., and Rappaport T. S., 1994, "Site-Specific Propagation Prediction for Wireless In-Building Personal Communication System Design," IEEE Transaction on Vehicular Technology, Vol. 43, No. 4, November

Sensor Technology Ltd., http://www.sensortech.ca/igniter.html

Shames I. H., and Dym C. L., 1991, Energy and Finite Element Methods in Structural Mechanics. Taylor & Francis, Levittown, PA

Shearwood C. and Yates R. B., 1997, "Development of an Electromagnetic Microgenerator," Electronics Letters, Vol. 33 No. 2, October

Shenck N. S. and Paradiso J. A., 2001, “Energy Scavenging With Shoe-Mounted Piezoelectrics,” IEEE 0272-1732/01

Sniegowski J.J., Guckel H. and Christenson T. R., 1999, “Performance Characteristic of Second Generation Polysilicon Resonanting Beam Force Transducers,” Solid-State Sensor and Actuator Workshop, 4th Technical Digest, Hilton Head Island, SC, IEEE, pp. 9-12

Starner T., 1996, “Human powered wearable computing,” IBM Syst. J., Vol. 35, pp. 618-629

Straser E. G., Kiremidjian A S., Law K. H. and Blume J. A., 2000, “A Framework for Health Monitoring of Structures,” Structures Congress and Exposition, ASCE, Philadephia, PA, May 8-10

Straser E. G., Kiremidjian A. S., Meng T. H., and Redlefsen L., 1998, “Modular, wireless network platform for monitoring structures,” Proceedings of the International Modal Analysis Conference – IMAC, pp. 450-456

The MOSIS Service, http://www.mosis.org/

Vittoz E. A., 1994, “Low-power design: Ways to approach the limits,” ISSCC 1994 Dig. Tech. Papers, Feb., pp.14-18

Warneke B. A., Scott M. D., Leibowitz B. S., Zhou L., Bellew C. L., Chediak J. A., Kahn J. M., Boser B. E., Pister K. S. J., 2002, “An Autonomous 16 mm^3 Solar-Powered Node for Distributed Wireless Sensor Networks,” IEEE 0-7803-7454-1/02

Weinberg M. S., 1999, “Working Equations for Piezoelectric Actuators and Sensors,” IEEE Journal of MEMS, Vol. 8, No. 4

Williams C.B., Pavic A., Crouch R.S., and Woods R.C., 1997, “Feasibility Study of Vibration-Electric Generator for Bridge Vibration Sensors,” IMAC-XVI Proceeding

Wu J., Quinn V., Bernstein G. H., 2001, “A simple, wireless powering scheme for MEMS devices,” Proceedings of SPIE Vol. 4559 (2001), MEMS Components and Applications for Industry, Automobiles, Aerospace, and Communication

Zhang H., Hayashida T., Takashi Yoshino, Shiro Ito and Yoji Nagasawa, 1999, “A Deterministic Model for UFH Radio Wave Propagation through Building Windows in Cellular Environments,” IEICE Transaction on Communication, Vol. E82-B, No. 6 June